Experiments and modeling of the coupled viscoelasticity and Mullins effect in filled rubber materials

Keven Alkhoury[†], Robert Ivko[†], Mokarram Hossain[‡]
Siva Nadimpalli[††], and Shawn A. Chester[†*]

[†]Mechanical Engineering
New Jersey Institute of Technology
Newark, NJ 07102 USA

[‡]Zienkiewicz Centre for Computational Engineering
College of Engineering, Bay Campus
Swansea University
Swansea, United Kingdom

[††] Department of Mechanical Engineering
Michigan State University
East Lansing, MI 48824 USA

April 17, 2024

Abstract

Filled rubber-like materials are widely used in engineering applications, and are known to exhibit a rate-dependent non-linear inelastic behavior and stress-softening, also known as the Mullins effect is frequently encountered. In this work, we characterized and modeled the constitutive response of a handful of commercially available filled rubber-like materials. We first perform a set of large-deformation uniaxial experiments at room temperature and at multiple rates. Those experimental findings are used to develop and calibrate a thermodynamically consistent constitutive model, which is then numerically implemented in a finite element package by writing a user material subroutine. The constitutive model is validated by comparing the results of an inhomogeneous experiment and simulation. A key finding of this work is that the mechanisms that cause the Mullins effect appear to be the main drivers of viscoelasticity in the materials used here.

Keywords: Inelastic; Large deformations; Mullins effect; Nonlinear; Viscoelastic.

*Corresponding author: shawn.a.chester@njit.edu

1 Introduction

Filled rubber-like materials also known as filled elastomers or filled viscoelastomers, consist of a polymer matrix embedded with stiff filler particles and are used in many applications ranging from industrial and consumer (Clark, 1981; Leblanc, 2002; Toopchi-Nezhad et al., 2008) to medical applications (Birmingham et al., 1998; Herrington et al., 2005). In general, filled viscoelastomers, are known to exhibit a rate-dependent non-linear inelastic behavior, where stress softening, also known as the Mullins effect is frequently encountered.

When discussing the mechanical behavior of materials exhibiting the Mullins effect, two terms describing the state of the material are necessary to understand — virgin, and preconditioned. Virgin material is a raw material without any prior loading history. Whereas preconditioned material is a material that has been mechanically cycled under displacement control numerous times. Preconditioning has been used to eliminate the Mullins effect (Dorfmann and Ogden, 2003, 2004; Diani et al., 2009), and therefore is often performed prior to testing or application. However, there remains significant ambiguity on how long the effects of preconditioning last in eliminating the Mullins effect.

The Mullins effect is most easily explained through a stress - stretch curve. As shown in Figure 1, when a virgin filled viscoelastomer is subjected to displacement controlled cyclic loading, the stress is expected to become softer during the reloading until the material reaches the previous maximum stretch, after that, the stress follows the prior loading path. This phenomenon was first intensively studied by Mullins (1948) more than 7 decades ago, yet, there is still no general agreement either on the physical source or on the mechanical modeling of this effect (Diani et al., 2009; Plagge and Klüppel, 2019).

Although the origin of this effect is yet to be determined, the mechanics literature has seen numerous experimental contributions, in which filled viscoelastomers, showed significant Mullins effect (cf. eg., Bouasse and Carrière, 1903; Harwood et al., 1965; Harwood and Payne, 1966; Lion, 1996; Bergström and Boyce, 2000; Hossain and Liao, 2020; Hossain et al., 2020; Liao et al., 2020b,a, 2021, and references within).

Furthermore, it is well known that the Mullins effect can be partially or fully recovered; and the rate and degree of recovery can be affected by various conditions such as filler type, temperature,

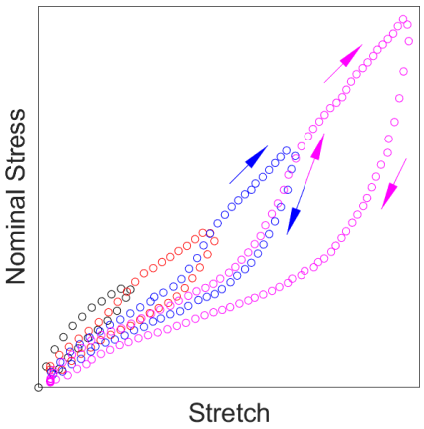

Figure 1: A schematic showing the Mullins effect. Each loading cycle, to increasing strain levels, is shown in a different color for clarity.

and solvent exposure (cf. eg., Mullins, 1948; Diani et al., 2009; Yan et al., 2010; Wang and Chester, 2018a; Chen et al., 2020, and references within). And while this work's main focus is not on the Mullins recovery specifically, it remains an important phenomenon that should not be neglected when modeling this class of materials.

There have been numerous attempts to model the Mullins effect based on phenomenological models and physical interpretations leading to micro-mechanical models. For example, one of the earliest phenomenological attempts was to describe the filled viscoelastomer as an isotropic two-phase system containing a hard phase and a soft phase, where the hard phase evolves into the soft phase upon stretching only if the stretch is greater than any previous maximum stretch (Mullins and Tobin, 1957, 1965; Harwood et al., 1965; Harwood and Payne, 1966). More contemporary models (Bergstrom and Boyce, 1999; Qi and Boyce, 2004) based on this early phenomenological concept were also developed and recently used by Wang and Chester (2018b) to model the combined viscoelasticity and Mullins effect in a filled elastomer. Another class of phenomenological models is built upon continuum damage mechanics (Simo, 1987; Miehe, 1995), or pseudo-elasticity (Ogden and Roxburgh, 1999; Dorfmann and Ogden, 2003, 2004) where a damage parameter capturing any physical phenomenon such chain and multichain damage, microstructural damage, microvoid formation, etc., evolves with the deformation (Diani et al., 2009). On the other hand, physical explanations involving micro-structural changes (Blanchard and Parkinson, 1952; Houwink, 1956; Bueche, 1960) that are typically based on the statistical mechanics of chain rupture or filler cluster

rupture lead to micro-mechanical models that have shown success (Bueche, 1960; Govindjee and Simo, 1991; Klüppel and Schramm, 2000; Marckmann et al., 2002).

Equally important, since filled viscoelastomers exhibit a rate-dependent behavior, which is typically influenced by the volume fraction of the filler particles (Payne, 1962; So and Chen, 1991; Lion, 1996), one should not forget to mention both phenomenological based (Lubliner, 1985; Simo, 1987; Holzapfel and Simo, 1996; Lion, 1997; Reese and Govindjee, 1998; Bergström and Boyce, 1998) and micro-mechanics based models (Green and Tobolsky, 1946; Miehe and Göktepe, 2005; Linder et al., 2011), that have been used to capture that rate-dependent behavior of these materials successfully.

In more recent efforts, Lu et al. (2017) characterized and modeled the behavior of soft materials exhibiting both viscoelasticity and Mullins effect. Reis et al. (2021), proposed a model for visco-hyperelastic materials with Mullins effect merging a phenomenological approach with a macromolecular one and were successfully able to predict the behavior of polyurethane elastomers undergoing intermediate deformations, up to a strain of $\approx 30\%$. Li et al. (2023) proposed a constitutive model that incorporates the Mullins effect and the magnetic-dependent nonlinear viscoelastic behavior of isotropic soft magnetorheological elastomers undergoing small deformations, up to a strain of $\approx 15\%$. Anssari-Benam et al. (2023) extended the theory of pseudo-elasticity to capture the permanent set and the induced anisotropy in the Mullins effect.

Our experimental investigations show a novel behavior not previously reported in the literature. We have experimentally found that the mechanisms that cause the Mullins effect appear to be the main drivers of viscoelasticity in the materials used here. We also found evidence that for some of the materials used, preconditioned samples exhibited recovery of the Mullins effect at room temperature.

Accordingly, the overall goal of this work is to determine the low to moderate rate constitutive behavior of filled viscoelastomers at room temperature while concurrently addressing the Mullins effect, large deformation viscoelasticity, and coupling between them. Toward that goal we have taken a combined experimental and modeling approach.

We have designed and conducted an experimental program that decouples each phenomenon in order to assess them separately as much as possible. Those experiments are broadly grouped as either virgin or preconditioned so that we can experimentally separate the underlying mechanisms

that affect the material behavior. Specifically we have used the filled materials Silicone DC745U, Buna 50A, Neoprene 50A, and Neoprene 70A (Vijayaram, 2009; Diani et al., 2009) for their many important applications across various fields (Lerman, 1989; Birmingham et al., 1998; Hashimoto et al., 1998).

For our modeling effort, we adopt and build upon the phenomenological approach of Qi and Boyce (2004) and assume that a typical filled viscoelastomer may be treated as composite material with rigid filler particles to capture the rate-independent behavior with the stress softening. To that we append the work of Linder et al. (2011) and employ their micromechanics motivated model to capture the viscous behavior of the investigated materials. Following our recent work (Wang and Chester, 2018b), we introduce a scalar internal variable that captures the complex stretch-stretch rate stiffening of the viscous response, as well as the asymmetric nearly rate-independent response during unloading. Thermal recovery of the Mullins effect is also incorporated by a basic Arrhenius function. The proposed model is then calibrated against uniaxial experiments using a nonlinear least square method, and is later numerically implemented as a user material subroutine (UMAT) in Abaqus/Standard (2023) and used for validation in a set of inhomogeneous deformation experiments.

The remainder of this paper is organized as follows. In Section 2, we report on our experimental methods for characterizing the quasi-static combined effects of the Mullins effect, its room temperature thermal recovery, and viscoelasticity, along with the accompanying results. In Section 3, we provide a summary of the experimental results that is later used to inform the model. In Section 4, we overview the constitutive framework. In Section 5, we present the constitutive model, which is then calibrated in Section 6. In Section 7, we validate our model. In Section 8, we provide concluding remarks.

2 Experiments

In this section we report on our experimental methods for characterizing the quasi-static combined effects of the Mullins effect, its room temperature thermal recovery, and viscoelasticity, along with the accompanying results.

2.1 Uniaxial experiment preliminaries

For a uniaxial experiment on filled viscoelastomers we employ two kinematic quantities, the stretch

$$\lambda = \frac{l}{l_0} = \frac{u + l_0}{l_0} = 1 + \frac{u}{l_0}\,, \tag{1}$$

and the stretch rate

$$\dot{\lambda} = \frac{\dot{u}}{l_0}\,, \tag{2}$$

where l is the instantaneous gauge length, l_0 is the initial gauge length, u is the displacement, and $\dot{u}$ is the load-frame velocity. We have chosen to perform our experiments under displacement control, and at a constant stretch rate. Therefore, we use (2) to prescribe the load frame velocity for a tension test at a constant stretch rate.

As is standard, the nominal, or engineering, stress P, is the force is divided by the initial cross-sectional area A_0

$$P = \frac{F}{A_0}\,. \tag{3}$$

2.2 Uniaxial experimental setup

We performed our uniaxial tests using an MTS Criterion Model 43 testing machine. A 500 N load cell (MTS Model LPB.502 D) is used to measure the force that is later used to calculate the stress. We use the non-contact Digital Image Correlation (DIC) software Vic2D (Correlated Solutions) which is integrated with a digital camera (FLIR Grasshopper3) to measure the deformation in our experiments. This is a standard practice for large deformations since measuring the deformation based on the crosshead displacement is known to be less accurate. Moreover, our DIC data acquisition system captures images simultaneously while taking force signal measurements, which is convenient when it comes to the post-processing since the deformation and force are synchronized in time.

2.3 Sample preparation

Prior to the experiments, tensile dog bone samples are extracted from the sheets using an ASTM D638-V cutting die. The nominal gauge section dimensions of our samples are 9.49 mm long and

3.18 mm wide. The Silicone DC745U samples were nominally 1 mm thick, Buna 50A samples were nominally 2.38 mm thick, and both Neoprene 50A and 70A were nominally 1.58 mm thick. The variety of thicknesses are a combination of what is commercially available and also operating within our load cell limits. The dimensions of samples are measured right before testing due to expected dimensional variations. Since DIC analysis requires contrast for accurate measurements, we apply a number of black dots using a paint marker on DC745U and white dots using a paint primer on Buna 50A and both Neoprene 50A and 70A.

2.4 Experimental plan

In general, filled viscoelastomers show a complex behavior where the Mullins effect and viscoelasticity take place concurrently. For that reason, and in order to have a comprehensive understanding of their behavior, we have designed an experimental program that decouples each phenomenon as much as possible in order to assess them separately. We note that all our experiments were performed at room temperature (24°C), and all results shown were repeated at least 3 times each to ensure repeatability.

When we use the term preconditioning, that means a sample was cycled (load and unload) for at least 6 cycles to the same stretch, typically larger than the maximum stretch expected in a future tensile test, unless otherwise specified, and then allowed to relax stress free for 24 hours before further testing. We observed that cycling the samples for more than 6 cycles had no further effect on the constitutive response, for all the investigated materials.

The experimental program is broken down into the following steps:

- A suite of experiments to probe the rate-independent behavior in the absence of viscoelasticity and the Mullins effect. For this, we perform large deformation quasi-static ($\dot{\lambda} = 10^{-4}\text{s}^{-1}$) uniaxial load/unload tests on preconditioned specimens.

- A suite of experiments to probe the Mullins effect in the absence of viscous effects. For this, we perform large deformation quasi-static ($\dot{\lambda} = 10^{-4}\text{s}^{-1}$) uniaxial load/unload/reload tests on virgin specimens.

- A suite of experiments to probe the rate-dependent behavior in the absence of the Mullins

effect. For this, we perform a set of uniaxial load/unload tests at various stretch rates ($\dot{\lambda} = 10^{-3}\text{s}^{-1}$, $\dot{\lambda} = 10^{-2}\text{s}^{-1}$, and $\dot{\lambda} = 10^{-1}\text{s}^{-1}$) on preconditioned samples.

- A suite of experiments to probe the overall rate-dependent behavior with both mechanisms of inelasticity active. For this, we perform a set of uniaxial load/unload/reload tests at various rates ($\dot{\lambda} = 10^{-3}\text{s}^{-1}$, $\dot{\lambda} = 10^{-2}\text{s}^{-1}$, and $\dot{\lambda} = 10^{-1}\text{s}^{-1}$), as well as multistep uniaxial relaxation tests on virgin specimens.

- A suite of experiments to probe the relationship between viscoelasticity and the Mullins effect:

  – We perform a set of multistep uniaxial relaxation tests on samples with different preconditioning stretches.

  – We perform uniaxial load/unload/reload tests on virgin samples, immediately followed by a preconditioning cycle, immediately followed by a repeat of the load/unload/reload cycles at different rates. These experiments are done purposefully to not allow any time for relaxation or recovery of the Mullins effect.

2.5 Quasi-static load/unload on preconditioned specimens

We performed quasi-static load/unload tensile tests on preconditioned samples at a prescribed stretch rate of $10^{-4}\,\text{s}^{-1}$ to have a baseline of the rate-independent behavior of all materials in the absence of both viscoelasticity and Mullins effect (Diani et al., 2009). While it is possible to go at a slower rate, it is not practical since the time each experiment would take becomes excessive. Figure 2 shows that preconditioned DC745U samples exhibits a typical near hyperelastic behavior under a quasi-static load/unload cycle, however, all other materials show some hysteresis, suggesting some inelastic mechanisms are still active at this rate.

2.6 Quasi-static load/unload/reload tests on virgin specimens

We performed quasi-static load/unload/reload tensile tests on virgin samples for all materials specifically to probe the Mullins effect. We load/unload/reload each material a number of times to increasing stretches, at a prescribed stretch rate of $10^{-4}\,\text{s}^{-1}$, the prescribed loading profile is schematically shown in Figure 3, where each cycle is in different color for clarity. Also, note that

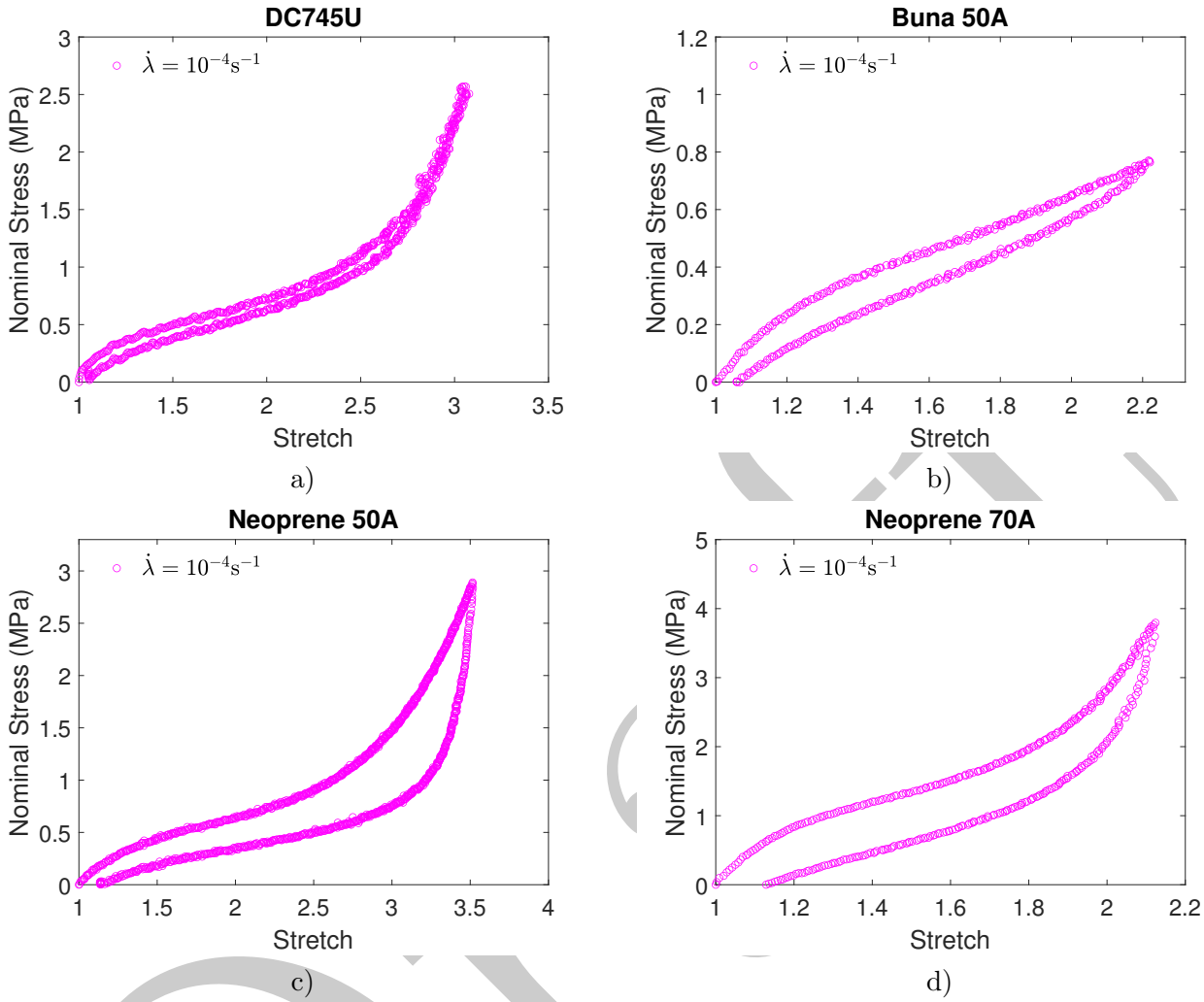

Figure 2: Quasi-static uniaxial load/unload tensile test result on preconditioned a) DC745U, b) Buna 50A, c) Neoprene 50A, and d) Neoprene 70A. Note the scale is not the same for each plot.

each unloading was reversed when the force signal reached zero, thus preventing the samples from going into compression or buckling.

The results of the quasi static load/unload/reload tensile experiments are shown in Figure 4. It can be clearly observed that all four materials exhibit the Mullins effect. After first loading a virgin specimen, it is clear that the specimen "softens" during the unloading. Then, upon reloading, the stress follows the previous unloading curve, until reaching the maximum stretch achieved in the first cycle, after which it "continues" the initial loading curve. The same behavior can be observed for the remaining load-unload cycles indicating the presence of stress-softening phenomenon also known as the Mullins effect.

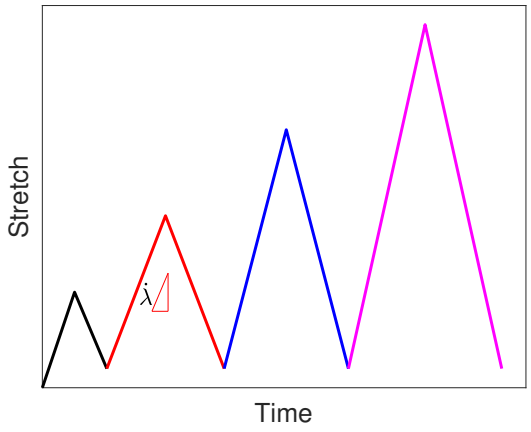

Figure 3: Schematic of the prescribed load/unload/reload stretch profile. Each cycle is in different color for clarity. Also, note that each unloading was reversed when the force signal reached zero, thus preventing the samples from going into compression or buckling.

2.7 Load/unload at different stretching rates on preconditioned specimens

In addition to quasi-static load/unload tensile tests on preconditioned samples, we also performed load/unload tensile tests on preconditioned samples at multiple prescribed stretch rates of $10^{-3}\,\mathrm{s}^{-1}$, $10^{-2}\,\mathrm{s}^{-1}$, and $10^{-1}\,\mathrm{s}^{-1}$, to probe the rate-dependent behavior of the materials while minimizing the Mullins effect as much as possible.

The results of the load/unload tensile tests on preconditioned samples are shown in Figure 5. Both preconditioned DC745U and Neoprene 50A show a rate-independent behavior, while both Buna 50A and Neoprene 70A show a rate-dependent behavior.[1] That along with the results previously shown in Section 2.5 suggests that both DC745U and Neoprene 50A are effectively rate-independent in the absence of the Mullins effect, suggesting that the mechanisms underlying the Mullins effect might be the major driver of the rate-dependency in those two materials.

2.8 Load/unload/reload at different stretch rates on virgin specimens

Furthermore, we performed load/unload/reload tensile tests on virgin samples for all materials to probe the overall rate-dependent behavior. The samples were loaded to increasing stretches and then unloaded, at prescribed stretch rates of $10^{-3}\,\mathrm{s}^{-1}$, $10^{-2}\,\mathrm{s}^{-1}$, and $10^{-1}\,\mathrm{s}^{-1}$, and then reloaded, with this cycle repeating 4 times. The prescribed loading profile is similar to what was used in

[1] As it will be revealed later, the observed rate-dependency may be due to recovery of the Mullins effect since the samples were tested 24 hours after preconditioning.

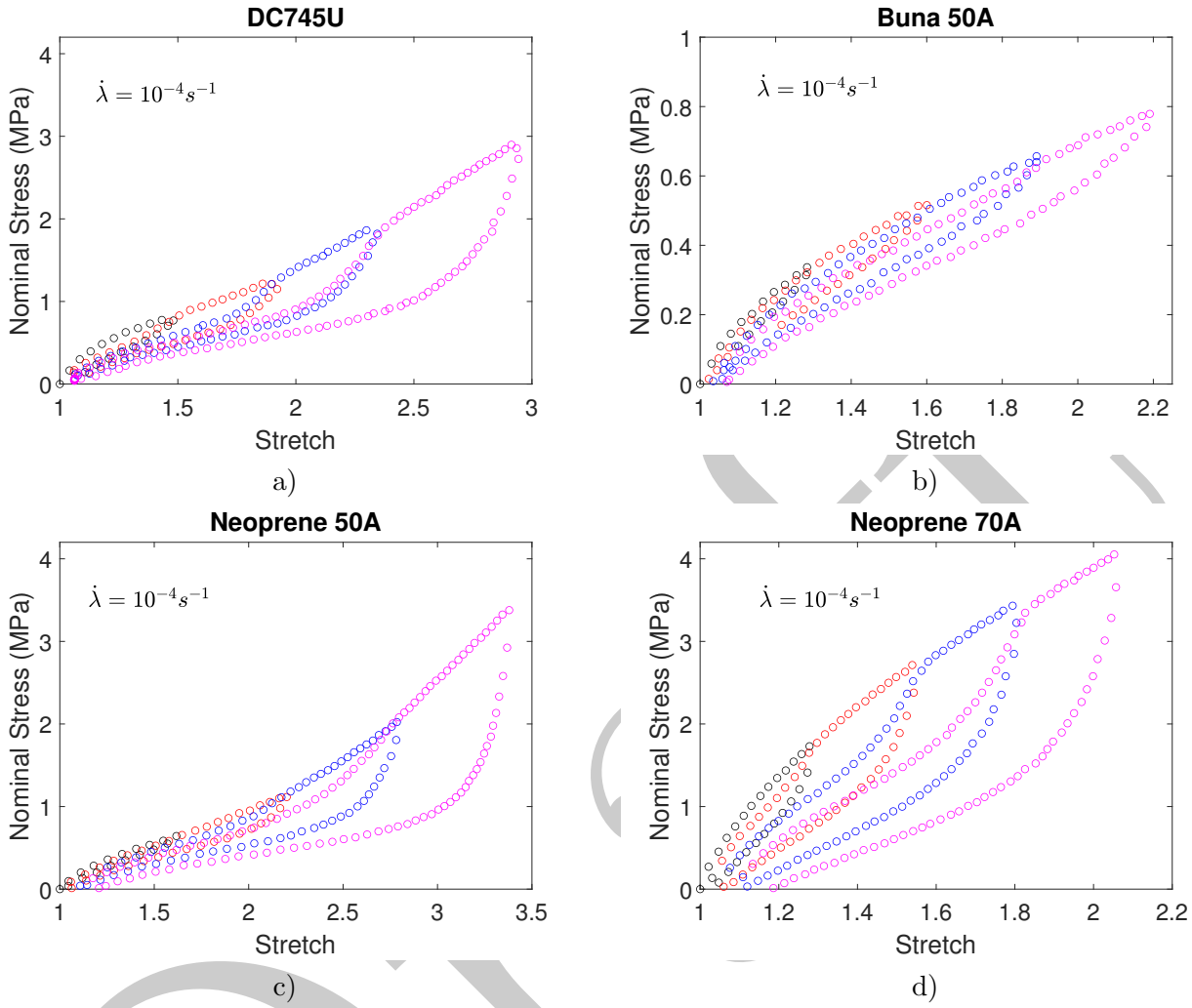

Figure 4: Quasi-static ($\dot{\lambda} = 10^{-4}\text{s}^{-1}$) uniaxial tensile test results on virgin specimens. a) DC745U, b) Buna 50A, c) Neoprene 50A, and d) Neoprene 70A. Note the scale is not the same for each plot, and each cycle is in different color for clarity, and corresponds to Figure 3.

Section 2.6, however now multiple rates are used.

The results of the load/unload/reload tensile experiments at multiple stretch rates, on virgin samples are shown in Figure 6. It can be clearly observed that all four materials exhibit the expected behavior of a filled viscoelastomer: Mullins effect, rate-dependence, and hysteresis.

2.9 Multi-step relaxation tests on virgin specimens

Multi-step relaxation experiments were also performed on virgin specimens to investigate the overall relaxation behavior for all materials. First, samples are loaded to a prescribed stretch, at a stretch rate of $\dot{\lambda} = 10^{-1}\,\text{s}^{-1}$. Once the prescribed stretch is reached, the crosshead is held fixed for 2000

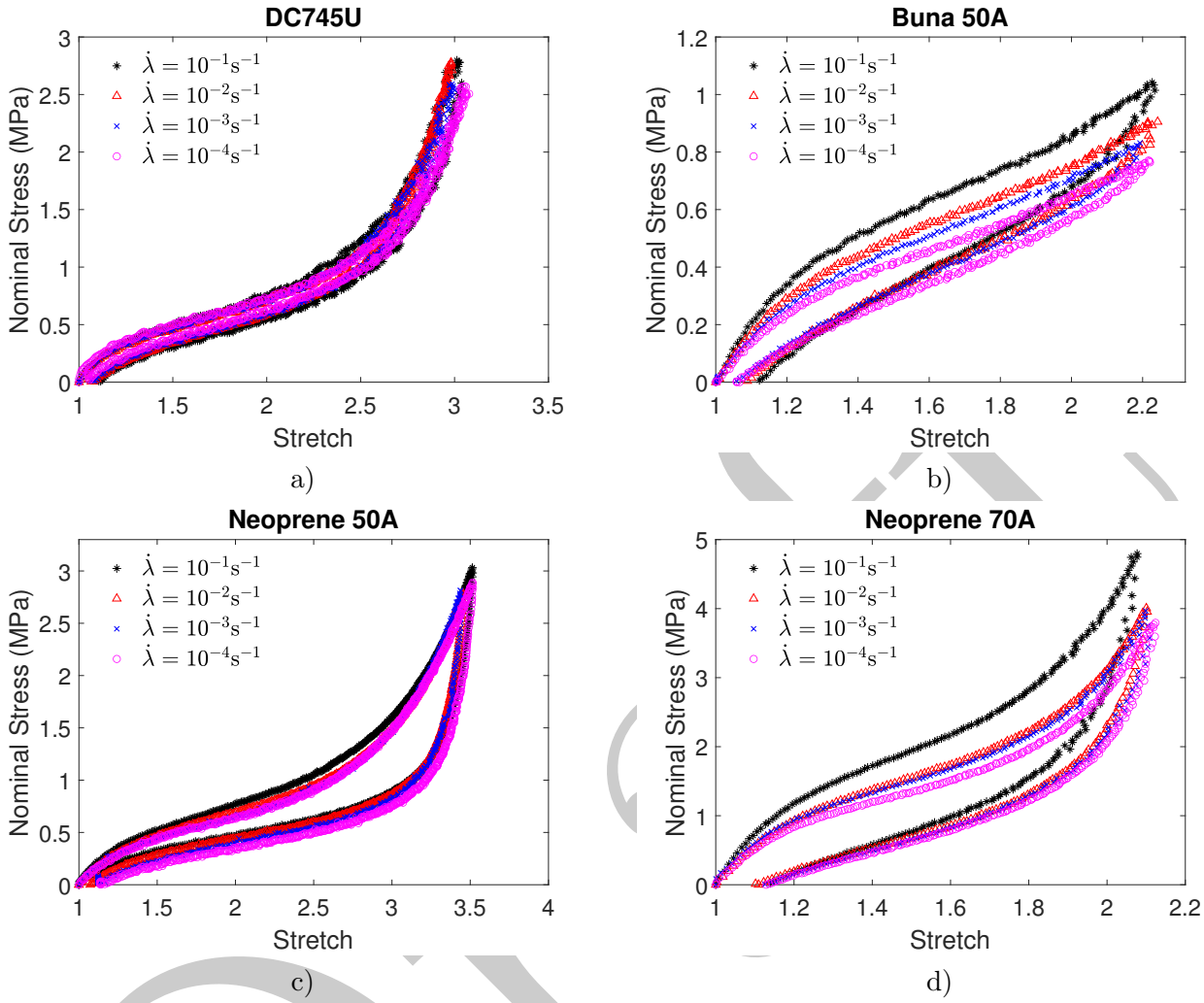

Figure 5: Uniaxial load/unload tensile results on preconditioned a) DC745U, b) Buna 50A, c) Neoprene 50A, and d) Neoprene 70A specimens at multiple stretch rates.

seconds, an amount of time that adequately probes the stress relaxation behavior of the tested materials, without the need for extended duration experiments. That procedure is then repeated multiple times for loading as well as unloading to perform the full multi-step relaxation test, with a loading profile schematically shown in Figure 7.

The results of the multi-step stress relaxation experiments are shown in Figure 8. Figures 8a, c, e, and g show the stress-stretch behavior during a multi-step relaxation test, while Figures 8b, d, f, and h show the stress-time behavior. These results clearly show that the stress approaches equilibrium over time within each step; decaying during loading, while staying nearly constant during unloading for DC745U, and slightly increasing for Buna 50A and both Neoprene 50A and

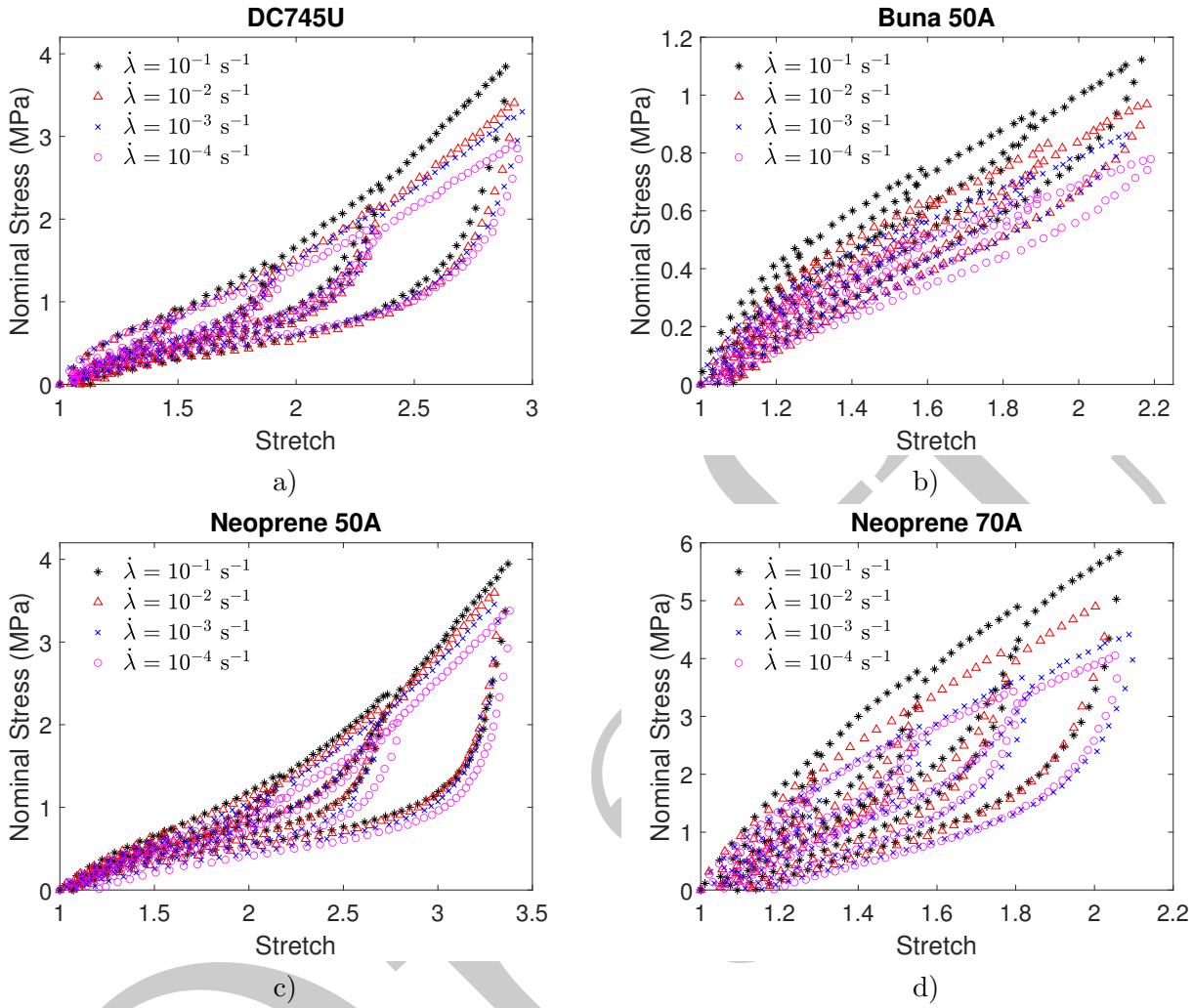

Figure 6: Uniaxial load/unload/reload tensile test results on virgin specimens at multiple stretch rates for a) DC745U, b) Buna 50A, c) Neoprene 50A, and d) Neoprene 70A.

70A which shows an asymmetric viscous response between loading and unloading of varying degree for all materials tested.

Further, the data shown in both Figure 6 and Figure 8 show that as the loading stretch is increased, there is a change in rate-dependence, therefore we have a stretch-dependent rate-dependence only during loading and not during unloading. In order to quantify this rather complex behavior, we begin by plotting only the loading portion of the curves from Figure 6 in Figure 9. What can be observed in Figure 9a, c, e, and g is that at low deformations all rates are atop each other, but as the deformation increases the apparent rate-dependence also changes. Building upon the analysis of rate-dependent plasticity in metallic materials, we plot the stress as a function of

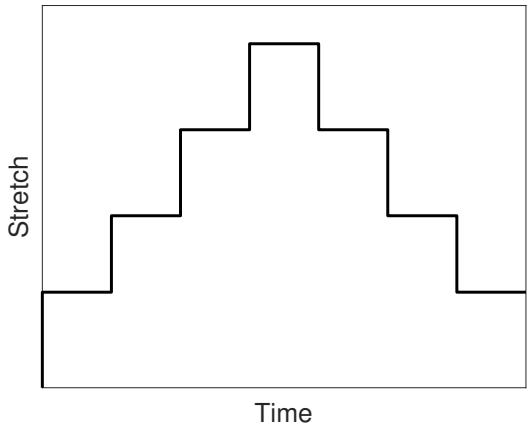

Figure 7: Schematic of the prescribed loading profile for a uniaxial multi-step relaxation test.

stretch rate as shown in Figure 9b, d, f, and h for numerous values of stretch. As the slope is typically known as the "rate-dependence," we can clearly see that the slope varies with increasing stretch and is not a constant, an indication from the experiments that this class of materials does indeed exhibit rate-dependence that changes with deformation, which is very typical for non-linear viscoelasticity (Amin et al., 2006, 2015; Hossain et al., 2020).

2.10 Experiments to probe the relationship between the Mullins effect and viscoelasticity

2.10.1 Multi-step relaxation tests on partially and fully preconditioned specimens

Following the same procedure described in Section 2.9, multistep relaxation tests were also performed on preconditioned samples having different maximum preconditioning stretches: (i) $\lambda^{\text{pre}} < \lambda^{\text{applied}}$; and (ii) $\lambda^{\text{pre}} > \lambda^{\text{applied}}$, to probe any relationship between the Mullins effect and viscoelasticity. In the first case, the preconditioning stretch is larger than the applied stretch, and in the second case, a more unconventional scenerio, the preconditioning stretch is lower than the applied stretch.

The results of these multi-step relaxation are shown in Figure 10. Figure 10 provides us with two major findings: (i) the level of the maximum stretch used for preconditioning not only has a role on the Mullins effect, but also affects the rate-dependent behavior of filled viscoelastomers, which has been previously reported in literature (Payne, 1962; So and Chen, 1991; Lion, 1996; Liao

et al., 2021); and (ii) all materials show an asymmetric rate-dependent behavior during unloading, specifically a less pronounced rate-dependency, suggesting that all mechanisms of inelasticity are majorly active during the loading steps and reduced during unloading.

While this immediate discussion that follows deals with the specifics for the response of DC745U, we note that the same behavior holds for all materials tested during loading. Taking a closer look at the first loading step for DC745U in Figures 10a and b where the applied stretch is $\lambda^{\text{applied}} = 1.5$, one can see that the virgin specimen shows a clear viscoelastic relaxation behavior, while both preconditioned samples show a nearly rate-independent response relaxing toward an equilibrium stress which is slightly higher for the samples preconditioned at a maximum stretch of $\lambda^{\text{pre}} = 2.4$. This result is expected since the maximum stretch used for preconditioning (either $\lambda^{\text{pre}} = 2.4$ or $\lambda^{\text{pre}} = 3.3$) is much higher than the applied stretch $\lambda^{\text{applied}} = 1.5$, and corroborates that the mechanisms responsible for the Mullins effect are tied to the mechanisms of viscoelasticity. This same trend holds in further increments in deformation, until nearing an applied uniaxial stretch of $\lambda^{\text{applied}} = 2.4$. Once nearing an applied uniaxial stretch of $\lambda^{\text{applied}} = 2.4$, we can see from Figures 10a and b that the samples preconditioned at $\lambda^{\text{pre}} = 2.4$ show a transitional behavior to a point where they start behaving like virgin samples, in other words, the Mullins effect has returned. Moreover, the specimens that were preconditioned at $\lambda^{\text{pre}} = 3.3$ ($\lambda^{\text{pre}} > \lambda^{\text{applied}}$) start showing some relaxation behavior which is significantly smaller than the other experiments.

Remarkably however, during unloading, the response for all samples can be classified into two groups, i) DC745U and Neoprene 50A showing a *nearly* rate-independent behavior, and ii) Buna 50A and Neoprene 70A showing some relaxation behavior. This suggests that the mechanism that underpins the Mullins effect and viscoelasticity is only active during loading and inactive during unloading for both DC745U and Neoprene 50A; while being active during loading and partially active during unloading for both Buna 50A and Neoprene 70A. Therefore, the main result from this suite of multi-step relaxation experiments shows that the mechanisms underlying the Mullins effect are contributors to what drives viscoelasticity in this class of materials.

Yet, while the results reported here suggest that the mechanisms responsible for the Mullins effect are the main driver of viscoelasticity, the presence of viscoelasticity for preconditioned Buna 50A and Neoprene 70A reported here and in Section 2.7 can be interpreted in multiple ways. It is well known in literature that the Mullins effect can be partially or even fully recovered, depending

on the material's structure and exposure conditions (cf. eg., Mullins, 1948; Diani et al., 2009; Yan et al., 2010; Wang and Chester, 2018a; Chen et al., 2020, and references within). Accordingly, to fully characterize the behavior, the next set of experiments will explicitly target recovery.

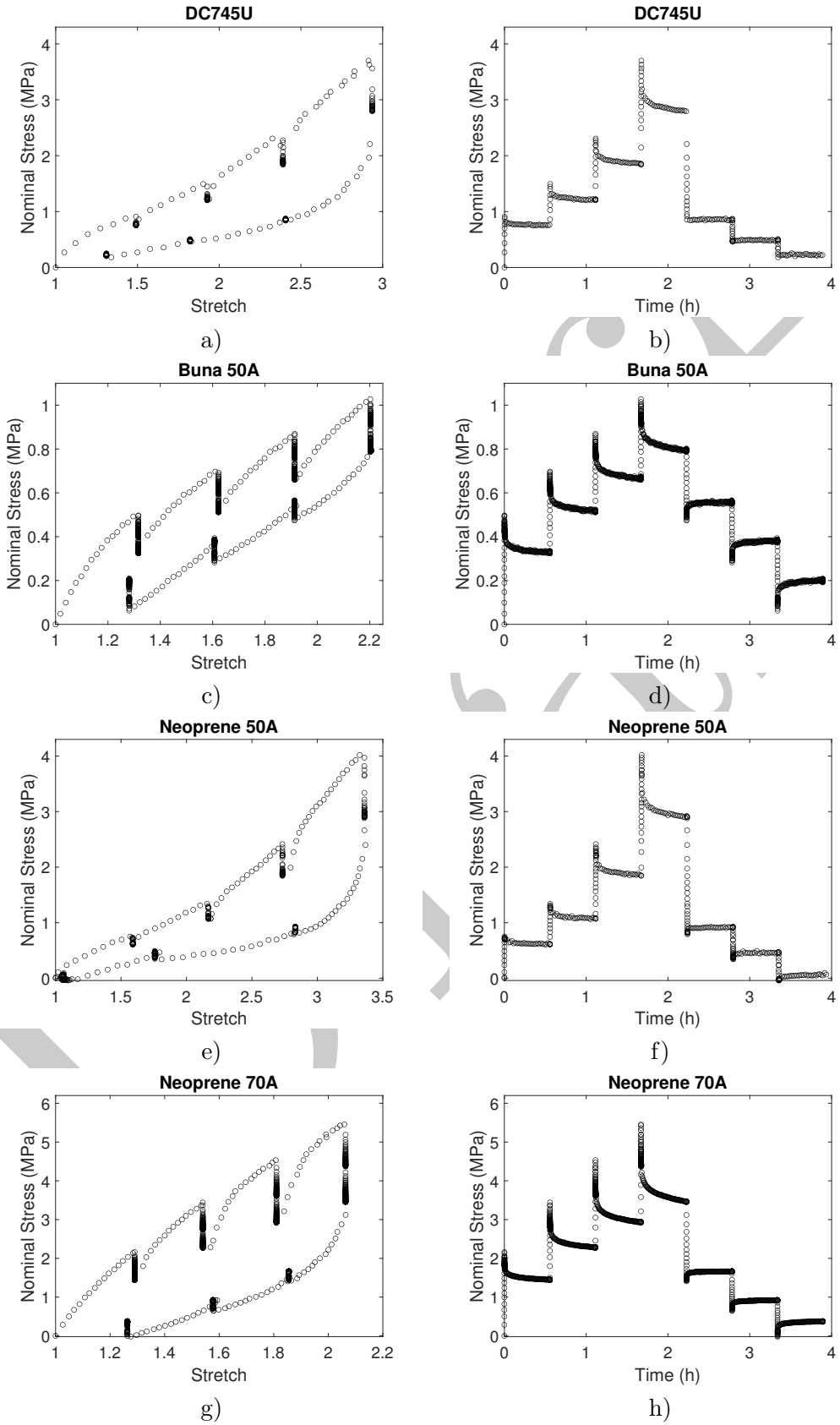

Figure 8: Uniaxial multi-step relaxation test on virgin specimens a, c, e, and g) nominal stress - stretch, and b, d, f, and h) nominal stress - time.

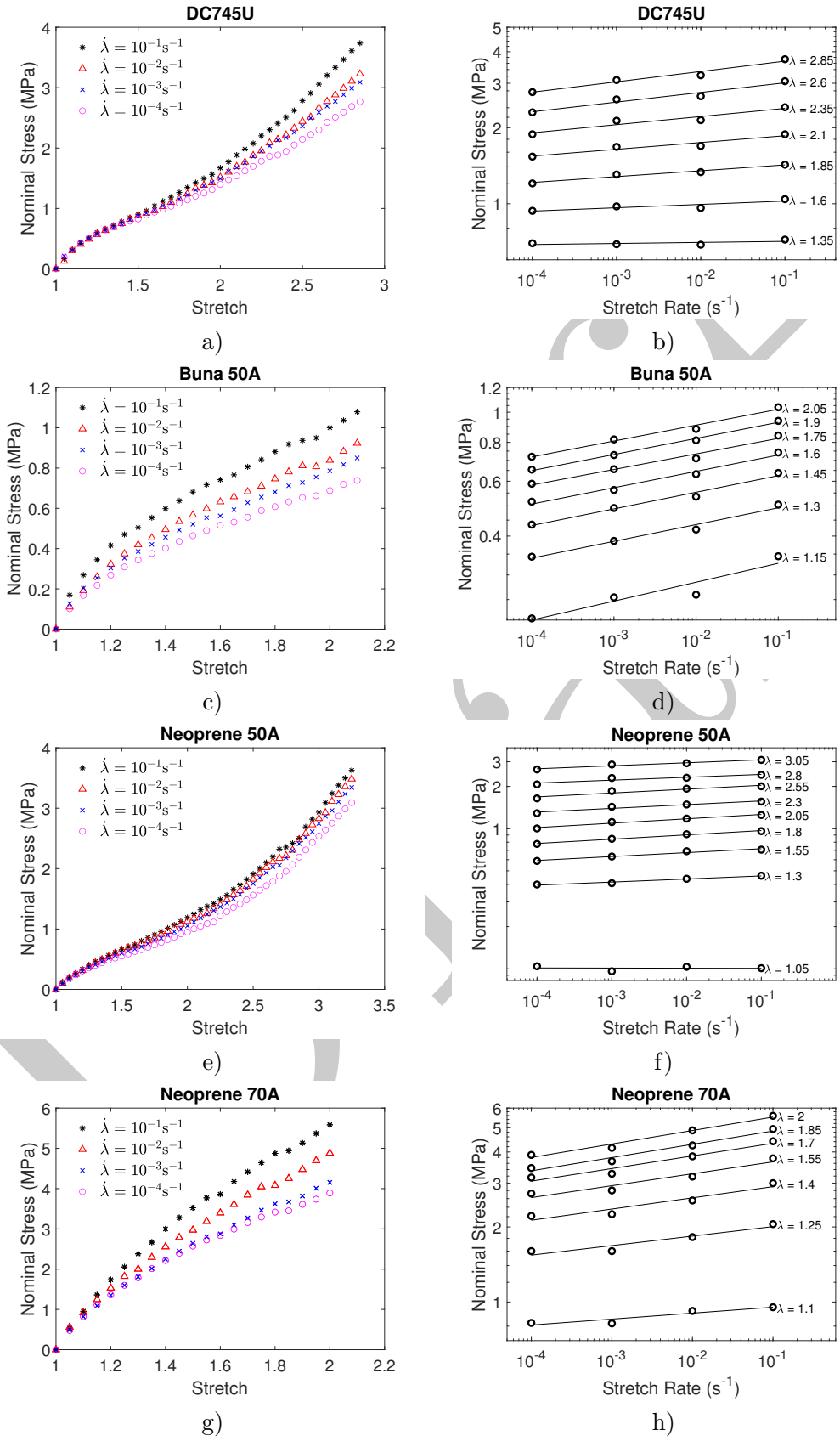

Figure 9: a, c, e and g) Load tensile test results on virgin specimens at multiple stretch rates, and b, d, f and h) log-log plot of the nominal stress as a function of stretch rate for different values of uniaxial stretch.

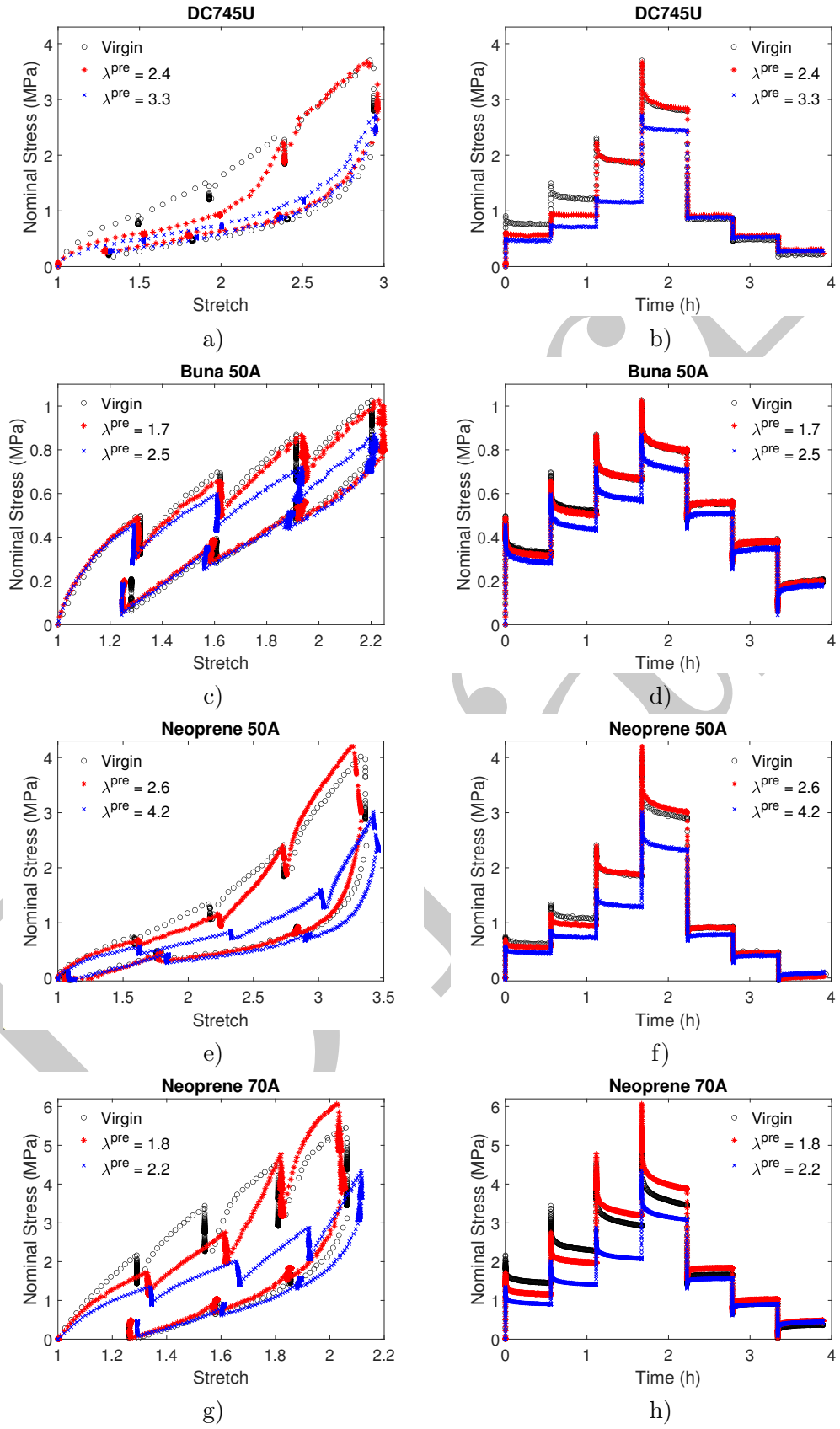

Figure 10: Uniaxial multi-step relaxation tests on virgin and preconditioned specimens, having different maximum preconditioning stretches λ^{pre}, a, c, e, and g) nominal stress - stretch, and b, d, f, and h) nominal stress - time.

2.10.2 Load/unload/reload tests on virgin, preconditioned, and stress-free recovered Buna 50A and Neoprene 70A specimens

As was mentioned previously, DC745U and Neoprene 50A did not exhibit a behavior that indicates there is any recovery of the Mullins effect. However the behavior of Buna 50A and Neoprene 70A exhibited noticeable rate-dependence after preconditioning. Therefore, to further investigate the relationship between the Mullins effect, *specifically* its recovery, and relation to viscoelasticity, we perform the following experiments on Buna 50A and Neoprene 70A:

- Step 1: Load/unload/reload tests on virgin samples at a rate of $10^{-1}\,\mathrm{s}^{-1}$ following the procedure from Section 2.8, immediately followed by 5 load/unload cycles to emulate "preconditioning," immediately followed by load/unload/reload tests at a rate of $10^{-1}\,\mathrm{s}^{-1}$, and $10^{-2}\,\mathrm{s}^{-1}$, respectively. We note that experiments were performed without allowing the samples to viscoelastically relax or recover the Mullins effect. These experiments allow us to compare the virgin response to the emulated "preconditioned" response (at two different rates) without allowing anytime for recovery, which gives us an insight on the nature of rate-dependency in the absence of Mullins effect.

- Step 2: Those samples are set aside stress-free for 24 hours at room temperature. This allows the samples to potentially recover the Mullins effect.

- Step 3: Finally, load/unload/reload tests at a rate of $10^{-1}\,\mathrm{s}^{-1}$, and $10^{-2}\,\mathrm{s}^{-1}$ are performed on those samples. These experiments will help us identify whether or not Mullins effect is recovering, which can be used to corroborate that the mechanisms behind the Mullins effect are a major driver of viscoelasticity.

Figure 11a and Figure 12a show the measured stretch-time history for the loading described in Step 1 above, and Figure 11b and Figure 12b are the corresponding measured stress-stretch response. Figure 11c and d and Figure 12c and d plot the data for the last two cycles as described in Step 1 above for the two stretch rates used simply for clarity. What can be observed from the data provided in Figure 11b, c, and d and Figure 12b, c, and d respectively, is that for Buna 50A and Neoprene 70A we find that there is a significant decrease in the rate-dependent response after the emulated "preconditioning" cycle. Additionally, the load/unload/reload response for the

last two cycles does not show any sign of Mullins effect, which once again highlights the coupling between Mullins mechanisms and viscoelasticity.

Figure 11e and Figure 12e show the measured stress-stretch response for Buna 50A and Neoprene 70A, respectively, at two different rates after allowing for 24 hours of recovery as described in Step 3 above, plotted atop of each other. We can clearly see increased rate-dependence when compared to Figure 11b and Figure 12b. In addition to the increased rate-dependence, we can also see some Mullins effect, which indicates that there is some recovery of the Mullins mechanisms in Buna 50A and Neoprene 70A at room temperature in just 24 hours. We calculate the percent recovery, which is taken to be the ratio of the stress in the second loading stretch to the stress in the initial loading stretch in the virgin material. Here, the fourth loading cycle from Figure 11c and Figure 12c after the emulated "preconditioned" case and the 24 hours relaxed were used to make the comparison to determine if there is any recovery taking place. What can be observed from Figure 11f and Figure 12f is that the Mullins effect partially recovers in Buna 50A and Neoprene 70A at room temperature after just 24 hours, supporting the fact that the Mullins and viscoelasticity are indeed coupled.

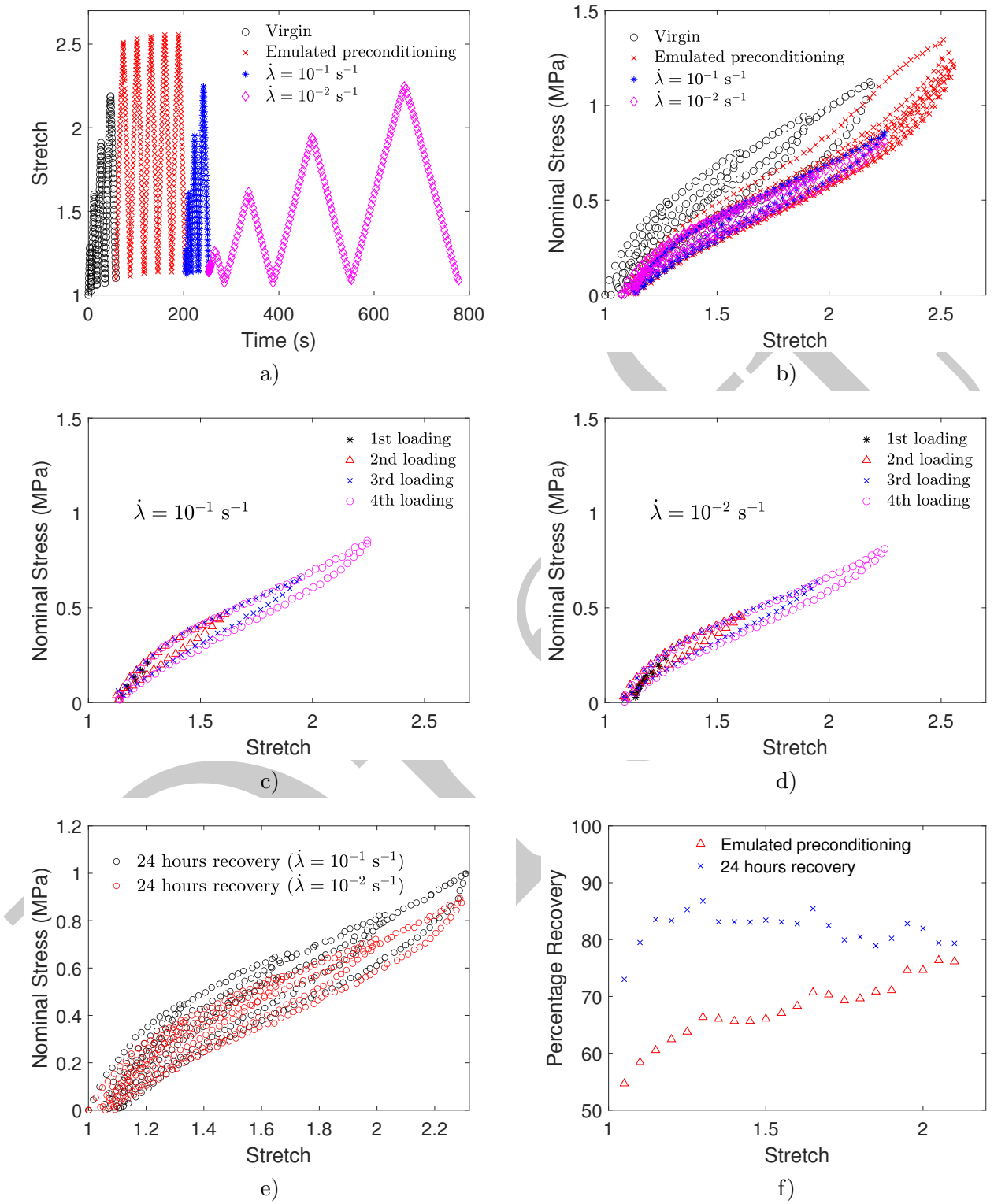

Figure 11: Results for Buna 50A. a) Measured load/unload/reload stretch profile with each cycle in a different color for clarity. And each unloading was reversed when the force signal reached zero. b) Corresponding stress-stretch results, c) load/unload/reload cycle at a rate of $10^{-1}\,\mathrm{s}^{-1}$ (blue in Figure 11a), d) load/unload/reload cycle at a rate of $10^{-2}\,\mathrm{s}^{-1}$ (magenta in Figure 11a), e) uniaxial load/unload/reload tensile test results for preconditioned specimens after a 24 hours stress free recovery at a stretch rate of $10^{-1}\,\mathrm{s}^{-1}$ and $10^{-2}\,\mathrm{s}^{-1}$, and f) measured percentage recovery.

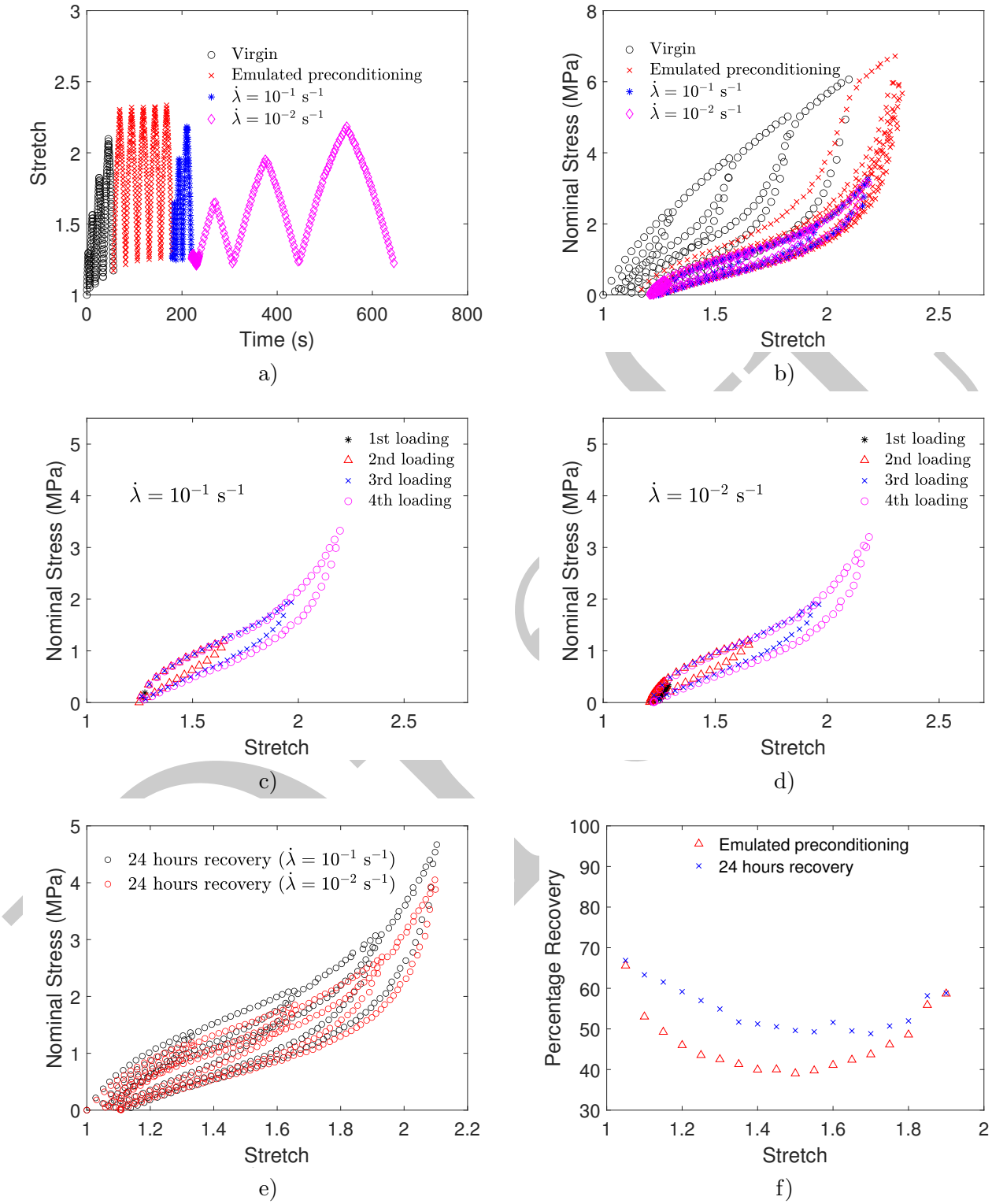

Figure 12: Results for Neoprene 70A. a) Measured load/unload/reload stretch profile with each cycle in a different color for clarity. And each unloading was reversed when the force signal reached zero. b) Corresponding stress-stretch results, c) load/unload/reload cycle at a rate of $10^{-1}\,\mathrm{s}^{-1}$ (blue in Figure 12a), d) load/unload/reload cycle at a rate of $10^{-2}\,\mathrm{s}^{-1}$ (magenta in Figure 12a), e) uniaxial load/unload/reload tensile test results for preconditioned specimens after a 24 hours stress free recovery at a stretch rate of $10^{-1}\,\mathrm{s}^{-1}$ and $10^{-2}\,\mathrm{s}^{-1}$, and f) measured percentage recovery.

3 Summary of the experimental results to inform the model

The experimental results provide crucial information to motivate our modeling efforts. The main takeaway from the experimental results are summarized in what follows:

- All materials tested exhibit the Mullins effect and concurrently inelastic behavior, such as rate-dependence, and hysteresis. Accordingly the constitutive model must include both Mullins effect and large deformation inelasticity.
- The inelastic mechanisms are more dominant during loading, where there exists a rate and stretch-dependent stiffening behavior. Accordingly, the constitutive model must be able to capture this phenomenon.
- The mechanisms that cause the Mullins effect partially recover at room temperature in just 24 hours for some materials. Accordingly the constitutive model must take recovery into account.
- Most importantly, the mechanisms that cause the Mullins effect appear to be the main drivers of viscoelasticity. Accordingly, unlike most prior work in this area of the literature, the constitutive model must couple the Mullins effect with viscoelasticity.

4 Continuum framework

In this section we overview the kinematics and the governing continuum level equations to describe the nonlinear mechanical behavior of the studied filled viscoelastomers. Since much of what follows here is built upon our recent work (Wang and Chester, 2018b), it is not cited each and every time, but acknowledged here.

4.1 Kinematics

Consider an undeformed body $\mathcal{B}_{\mathrm{R}}$ identified with the region of space it occupies in a fixed reference configuration, and denote by $\mathbf{x}_{\mathrm{R}}$ an arbitrary material point of $\mathcal{B}_{\mathrm{R}}$. The referential body $\mathcal{B}_{\mathrm{R}}$ then undergoes a motion $\mathbf{x} = \boldsymbol{\chi}(\mathbf{x}_{\mathrm{R}}, t)$ to the deformed body $\mathcal{B}_t$ with deformation gradient given by

$$\mathbf{F} = \nabla\boldsymbol{\chi}, \quad \text{such that} \quad J = \det \mathbf{F} > 0. \tag{4}$$

The right and left Cauchy-Green deformation tensors are given by

$$\mathbf{C} = \mathbf{F}^{\top}\mathbf{F}\,, \tag{5}$$

and

$$\mathbf{B} = \mathbf{F}\mathbf{F}^{\top}\,. \tag{6}$$

Also, the polar decomposition of the deformation gradient

$$\mathbf{F} = \mathbf{R}\mathbf{U} \tag{7}$$

into a rotation $\mathbf{R}$, and a symmetric stretch $\mathbf{U}$ is well known in the literature.

We assume that the material is *nearly*-incompressible, and introduce the distortional and volumetric parts of the deformation gradient, defined as

$$\mathbf{F}_{\text{dis}} = J^{-1/3}\mathbf{F} \quad \text{where} \quad \det \mathbf{F}_{\text{dis}} = 1\,, \tag{8}$$

and

$$\mathbf{F}_{\text{vol}} = J^{1/3}\mathbf{I} \quad \text{where} \quad \det \mathbf{F}_{\text{vol}} = J\,, \tag{9}$$

so that

$$\mathbf{F} = \mathbf{F}_{\text{dis}}\mathbf{F}_{\text{vol}}\,. \tag{10}$$

The corresponding distortional right and left Cauchy-Green deformation tensors are then

$$\mathbf{C}_{\text{dis}} = \mathbf{F}_{\text{dis}}^{\top}\mathbf{F}_{\text{dis}} = J^{-2/3}\mathbf{C}\,, \tag{11}$$

and

$$\mathbf{B}_{\text{dis}} = \mathbf{F}_{\text{dis}}\mathbf{F}_{\text{dis}}^{\top} = J^{-2/3}\mathbf{B}\,. \tag{12}$$

4.2 Stress softening variables

Building upon literature (Mullins and Tobin, 1957, 1965; Harwood et al., 1965; Harwood and Payne, 1966), and following our recent work (Wang and Chester, 2018b), we treat filled viscoelastomers

as a soft polymer matrix filled with stiff filler particles where the filler volume fraction is denoted by ν_f, and the volume fraction of soft polymeric domain is $\nu_s = 1 - \nu_f$. As is typical, the virgin material is assumed to initially have primarily hard regions that transform to soft with deformation.

Additionally, according to Mullins and Tobin (1957), when filled viscoelastomers undergo an arbitrary deformation, the hard filler accommodates much less of the overall deformation than the soft rubber matrix. Therefore, an amplified stretch

$$\Lambda = \sqrt{X(\bar{\lambda}^2 - 1) + 1} \tag{13}$$

is used as a deformation measure for the the polymeric matrix, where X is an amplification factor, and $\bar{\lambda}$ is the effective stretch given by

$$\bar{\lambda} = \sqrt{\operatorname{tr} \mathbf{C}_{\text{dis}}/3}\,. \tag{14}$$

As is typical, the amplification factor X depends on the soft volume fraction ν_s and the shape of the filler particles. In this work we assume the following form (Guth, 1945)

$$X = 1 + 3.5(1 - \nu_s) + 18(1 - \nu_s)^2\,. \tag{15}$$

4.3 Balance of forces and moments

Neglecting inertial effects, the balance of forces and moments in the deformed body $\mathcal{B}_t$ are expressed as

$$\operatorname{div}\mathbf{T} + \mathbf{b} = \mathbf{0} \quad \text{and} \quad \mathbf{T} = \mathbf{T}^\top, \tag{16}$$

where $\mathbf{T}$ is the Cauchy stress and $\mathbf{b}$ the body force. As standard, (16) serves as the governing partial differential equation (PDE).

5 Constitutive equations

Making use of the experimental findings from Section 2, and following our earlier work and common practice in the literature of viscoelastomers (Reese and Govindjee, 1998; Bergström and Boyce,

1998; Wang and Chester, 2018b), this section summarizes the specific constitutive equations for modeling the behavior of the filled viscoelastomers used in this work.

5.1 Free energy

We take the free energy density per unit reference volume to be additively decomposed into two contributions

$$\hat{\psi}_{\mathrm{R}}(\mathbf{C}, \nu_s, \mathbf{A}^{(\gamma)}) = \hat{\psi}_{\mathrm{R}}^{\mathrm{RI}}(\mathbf{C}_{\mathrm{dis}}, J, \nu_s) + \sum_{\gamma} \hat{\psi}_{\mathrm{R}}^{\mathrm{RD}(\gamma)}(\mathbf{C}_{\mathrm{dis}}, \nu_s, \mathbf{A}^{(\gamma)}) \,, \tag{17}$$

where $\hat{\psi}_{\mathrm{R}}^{\mathrm{RI}}(\mathbf{C}_{\mathrm{dis}}, J, \nu_s)$ is the rate-independent contribution, and $\sum_{\gamma} \hat{\psi}_{\mathrm{R}}^{\mathrm{RD}(\gamma)}(\mathbf{C}_{\mathrm{dis}}, \nu_s, \mathbf{A}^{(\gamma)})$ is the overall rate-dependent contribution employing γ viscous mechanisms using tensorial internal variables $\mathbf{A}^{(\gamma)}$.[2]

5.1.1 Rate-independent contribution to the free energy

For the rate-independent contribution to the free energy we adopt the work of Qi and Boyce (2004) by assuming that a typical filled viscoelastomer material may be treated as composite material with rigid filler particles which have the following form

$$\hat{\psi}_{\mathrm{R}}^{\mathrm{RI}} = \nu_s G_0^{\mathrm{RI}} {\lambda_L}^2 \left[\left(\frac{\Lambda}{\lambda_L} \right) \beta + \ln \left(\frac{\beta}{\sinh \beta} \right) - \left(\frac{1}{\lambda_L} \right) \beta_0 - \ln \left(\frac{\beta_0}{\sinh \beta_0} \right) \right] + \frac{1}{2} K (\ln J)^2 \,, \tag{18}$$

where ν_s is the soft volume fraction, G_0^{RI} is the initial shear modulus, λ_L is the locking stretch, and Λ is the amplified stretch previously described in (13) . Moreover, β and β_0 are functions given by

$$\beta = \mathcal{L}^{-1} \left(\frac{\Lambda}{\lambda_L} \right) \quad \text{and} \quad \beta_0 = \mathcal{L}^{-1} \left(\frac{1}{\lambda_L} \right) , \tag{19}$$

where $\mathcal{L}^{-1}$ is the inverse of the Langevin function, $\mathcal{L}(\bullet) = \coth(\bullet) - 1/(\bullet)$. K is the bulk modulus used to approximate the *near-incompressible* conditions and is assumed to be three orders of magnitude greater than the shear modulus G_0^{RI} (i.e., $K = 10^3 G_0^{\mathrm{RI}}$).

[2]We acknowledge that $\hat{\psi}_{\mathrm{R}}^{\mathrm{RI}}(\mathbf{C}_{\mathrm{dis}}, J, \nu_s)$ is not purely rate-independent as the evolution of ν_s is driven in part by the deformation rate. However, this breakdown into rate-independent and rate-dependent is the most common found in the literature, and thus we continue to use it here.

5.1.2 Rate-dependent contribution to the free energy

For the rate-dependent free energy, we follow the micro-mechanically motived work of Linder et al. (2011), which for each viscous mechanism γ takes the form

$$\hat{\psi}_{\mathrm{R}}^{\mathrm{RD}(\gamma)} = \frac{1}{2} G^{\mathrm{RD}(\gamma)} \left[\left(\mathbf{A}^{(\gamma)} : \mathbf{C}_{\mathrm{dis}} - 3 \right) - \ln \left(\det \mathbf{A}^{(\gamma)} \right) \right] , \tag{20}$$

where $G^{\mathrm{RD}(\gamma)}$ are shear moduli for each viscous mechanism γ.

Because our experimental results discussed in Section 2 show an asymmetric combined stretch-stretch rate stiffening, we implement the following functional form for the rate-dependent moduli to capture this rather complex behavior. We assume the form

$$G^{\mathrm{RD}(\gamma)} = (1 - \nu_s) \varphi G_0^{\mathrm{RD}(\gamma)} , \tag{21}$$

where $G_0^{\mathrm{RD}(\gamma)}$ is the ground state rate-dependent shear modulus for each γ. Here, the term $(1 - \nu_s)$ is introduced in (21) to capture the experimentally observed behavior that the viscoelasticity is tied to, if not driven by, the mechanisms that cause the Mullins effect. Accordingly, as a material point transitions between hard to soft, the affects of viscoelasticity are diminished. We emphasize that while $1 - \nu_s = \nu_f$, represents the filler volume fraction, we do not intend that the filler is deforming and accounting for this contribution to the free energy, it is simply a convenient phenomenological form. Also, φ is a scalar internal variable that acts on the viscous moduli to capture the asymmetric rate- and-stretch dependent stiffening experimentally observed in the rate-dependent response between the loading and the unloading. A discussion on the evolution of each $\mathbf{A}^{(\gamma)}$, ν_s and φ is presented in Section 5.3.

5.2 Cauchy stress

Based on thermodynamic restrictions, straightforward calculations provide the Cauchy stress $\mathbf{T}$ in the form

$$\mathbf{T} = J^{-1}\mathbf{F}\left(2\frac{\partial\hat{\psi}_{\mathrm{R}}}{\partial\mathbf{C}}\right)\mathbf{F}^{\top} = \underbrace{J^{-1}\left[G^{\mathrm{RI}}\left(\mathbf{B}_{\mathrm{dis}}\right)_0 + K\left(\ln J\right)\mathbf{1}\right]}_{\text{Rate-independent contribution}} + \underbrace{J^{-1}\sum_{\gamma} G^{\mathrm{RD}(\gamma)}\left[\mathbf{F}_{\mathrm{dis}}\mathbf{A}^{(\gamma)}\mathbf{F}_{\mathrm{dis}}^{\top} - \tfrac{1}{3}\left(\mathbf{A}^{(\gamma)} : \mathbf{C}_{\mathrm{dis}}\right)\mathbf{1}\right]}_{\text{Rate-dependent contribution}}, \quad (22)$$

where the rate-independent shear modulus $G^{\mathrm{RI}} = \nu_s X G_0^{\mathrm{RI}}\left(\frac{\lambda_L}{3\Lambda}\right)\mathcal{L}^{-1}\left(\frac{\Lambda}{\lambda_L}\right)$ is a function of the amplified stretch and stress softening variables.

5.3 Evolution equations

In what follows, we present a set of evolution equations that allow us to model the observed behavior that was summarized in Section 3. Specifically, we present an evolution equation of the soft volume fraction, the evolution of the tensorial internal variables $\mathbf{A}^{(\gamma)}$, used to capture the rate-dependent behavior, along with an evolution equation of the asymmetric parameter φ, to capture the asymmetric response between loading and unloading.

5.3.1 Evolution of the soft domain volume fraction ν_s

Extending on our previous work (Wang and Chester, 2018a), we take the evolution of the soft domain fraction to be

$$\dot{\nu_s} = d + r \qquad \text{with} \qquad \nu_s(\mathbf{x}_{\mathrm{R}}, t = 0) = \nu_{s0}\,, \quad (23)$$

where d and r are intended to model the rate of deformation-induced softening and the rate of static recovery, respectively.[3]

We adopt the phenomenological model proposed by Qi and Boyce (2004) for the evolution

[3]It is important to mention that although Mullins recovery can take place in a non-stress-free state, we have not considered that here due to limited experimental data.

equation for the soft volume fraction ν_s to describe the transformation from hard to soft phases

$$d = A(\nu_{ss} - \nu_s)\frac{\lambda_L - 1}{(\lambda_L - \Lambda^{\max})^2}\dot{\Lambda}^{\max}\,, \qquad \nu_s(\mathbf{x}_{\mathrm{R}}, t = 0) = \nu_{s0} \tag{24}$$

with

$$\dot{\Lambda}^{\max} = \begin{cases} \dot{\Lambda}, & \Lambda = \Lambda^{\max}\,, \\ f(\Lambda) & \Lambda < \Lambda^{\max}\,, \end{cases} \tag{25}$$

and A a material parameter. Additionally, (24) states that as ν_s approaches the steady state saturation value of ν_{ss} whenever $\dot{\Lambda} \neq 0$ starting from an initial condition ν_{s0} in the virgin state. Here, $f(\Lambda)$ is a new contribution that allows $\Lambda^{\max}$ to recover to its virgin state value in the absence of the deformation-induced softening, that is, when the current amplified stretch is less than the previous maximum stretch in the material. A particular constitutive form will be shortly specified. Moreover, according to Qi and Boyce (2004), ν_s approaches its steady state saturation value ν_{ss} faster than $\Lambda^{\max}$ approaches λ_L, for that reason, $\dot{\nu_s}$ will always become dormant prior to chain locking preventing any associated numerical issues.

Next, motivated by the existing literature and our previous work (Mullins, 1948; Diani et al., 2009; Wang and Chester, 2018a), we adopt the temperature-dependent Arrhenius form to model recovery, such that

$$r = r_0 \exp\left\{-\frac{Q}{R\theta}\right\}|\nu_* - \nu_s|\,, \qquad \text{with} \qquad \nu_* = \hat{\nu_*}(\theta)\,, \tag{26}$$

where $r_0 \leq 0$ is a pre-exponential factor, Q is an activation energy, R is the gas constant, and ν_* is a temperature-dependent saturation value of the recoverable soft domain fraction. Since this work only focuses on the constitutive response at room temperature, (26) can be simplified to

$$r = R_0|\nu_* - \nu_s|\,, \tag{27}$$

where $R_0 = r_0 \exp\left\{-\frac{Q}{R\theta}\right\}$ is a negative lumped parameter ($R_0 \leq 0$). Lastly, to capture the recovery of $\Lambda^{\max}$ we specialize $f(\Lambda)$ in $(25)_2$ such that $f(\Lambda) = R_0(\Lambda - 1)$ and the rate of recovery is the same as used for the soft volume fraction.

5.3.2 Evolution of the tensorial internal variables $\mathbf{A}^{(\gamma)}$

The evolution equation of each tensorial state dependent variable $\mathbf{A}^{(\gamma)}$ is given in the form

$$\dot{\mathbf{A}}^{(\gamma)} = \frac{1}{\tau^{(\gamma)}} \left(\mathbf{C}_{\text{dis}}^{-1} - \mathbf{A}^{(\gamma)} \right), \quad \mathbf{A}\left(\mathbf{x}_{\text{R}}, t = 0\right) = \mathbf{1}\,, \tag{28}$$

where $\tau^{(\gamma)}$ is relaxation time for each viscous mechanism γ. This form is a linear evolution equation and shows that each tensorial state dependent variable $\mathbf{A}^{(\gamma)}$ advances towards the current $\mathbf{C}_{\text{dis}}^{-1}$ with a relaxation time of $\tau^{(\gamma)}$.

5.3.3 Evolution of the asymmetric parameter φ

In order to capture the observed viscous stretch-stretch rate stiffening and the asymmetric inelastic response between loading and unloading, a dimensionless scalar parameter φ was previously introduced in (21). Building upon the recent work (Mao et al., 2017; Wang and Chester, 2018b), φ evolves with the amplified stretch rate $\dot{\Lambda}$, and the evolution equation is given by

$$\dot{\varphi} = B \mid \varphi_* - \varphi \mid^n \dot{\Lambda}\,, \tag{29}$$

where B ≥ 0 is a material parameter that controls the rate at which $\dot{\varphi}$ evolves, n controls the shape of the evolution, and

$$\varphi_* = \begin{cases} \left(1 - \dfrac{\Lambda}{D}\right)^{-p} \left(\dfrac{\dot{\Lambda}}{\dot{\Lambda}_0}\right)^{a\Lambda} & \text{when loading (i.e., } \dot{\Lambda} \geq 0\text{)} \\ 0 & \text{when unloading (i.e., } \dot{\Lambda} < 0\text{)}\,. \end{cases} \tag{30}$$

controls the value φ evolves toward. The parameter $D > 1$ controls the stretch dependent stiffening, the parameter p controls the shape and magnitude of stiffening. $\dot{\Lambda}_0$ is a reference amplified stretch rate is typically the slowest amplified stretch rate, and a is a rate-dependent parameter.

5.4 Specialized constitutive equations for uniaxial tension

In the special case of uniaxial tension, and assuming incompressibility, the constitutive model is simplified to a one-dimensional set of equations. In this special case the effective stretch is given

by

$$\bar{\lambda} = \sqrt{\frac{1}{3}\left(\lambda^2 + \frac{2}{\lambda}\right)}, \tag{31}$$

and the Cauchy stress takes the form

$$\sigma = \underbrace{G^{\mathrm{RI}}\left[\lambda^2 - \frac{1}{\lambda}\right]}_{\text{Rate-independent contribution}} + \underbrace{\sum_{\gamma} G^{\mathrm{RD}(\gamma)}\left[\lambda^2 A^{(\gamma)} - \frac{1}{\lambda\sqrt{A^{(\gamma)}}}\right]}_{\text{Rate-dependent contribution}}, \tag{32}$$

where σ is the Cauchy stress component in the loading direction. Further, the evolution of each $A^{(\gamma)}$ is given by

$$\dot{A}^{(\gamma)} = \frac{1}{\tau^{(\gamma)}}\left(\lambda^{-2} - A^{(\gamma)}\right). \tag{33}$$

Lastly, the nominal stress is given by

$$P = \underbrace{G^{\mathrm{RI}}\left[\lambda - \frac{1}{\lambda^2}\right]}_{\text{Rate-independent contribution}} + \underbrace{\sum_{\gamma} G^{\mathrm{RD}(\gamma)}\left[\lambda A^{(\gamma)} - \frac{1}{\lambda^2\sqrt{A^{(\gamma)}}}\right]}_{\text{Rate-dependent contribution}} \tag{34}$$

and can be used to directly compare with our experimental results, as well as for calibration.

6 Calibration

We note that before starting with the calibration process, the specialized constitutive equations for uniaxial tension provided in Section 5.4 are implemented in MATLAB, where we make use of the built-in functions `lsqnonlin` and `MultiStart` to perform the nonlinear least squares.

The constitutive model calibration process consists of two steps that build upon each other. We first calibrate the rate-independent parameters along with the parameters related to the Mullins effect, including the recovery term using quasi-static experimental data. We then hold those parameters fixed and move onto calibration of the rate-dependent parameters using experiments from the other stretch rates and the multi-step relaxation.

First, we calibrate the specialized constitutive model against the quasi-static load/unload/reload experiments on virgin specimens to obtain the rate-independent parameters along with the parameters related to the Mullins effect. The calibrated model along with the experimental data for virgin

materials quasi-static conditions is shown in Figures 13a, 14a, 15a, and 16a, and the calibrated parameters are tabulated in Tables 1, 2, 3, and 4. Lastly, we assume that $\nu_* = \nu_{s0}$, due to the lack of data on Mullins recovery for the tested materials.

Next, holding the previously calibrated parameters fixed, we perform a least squares fit to both the load/unload/reload at different rates, and relaxation experiments of virgin specimens to calibrate the rate-dependent contribution. In order to capture the material behavior, we use two viscous mechanism ($\gamma = 2$) for the rate-dependent contribution since we found that having more viscous mechanisms did not show any improvement. The calibrated model along with the experimental data for virgin materials can be observed in Figures 13b-d, 14b-d, 15b-d, 16b-d with the calibrated parameters provided in Tables 1, 2, 3, and 4.

The main observation is that our model can reasonably reproduce the overall behavior of all materials tested here, including the Mullins effect, rate-dependency and the asymmetry between loading and unloading, however is more accurate with the load-unload than relaxation experiments. Specifically, given the provided material parameters, our model better reproduces the cyclic load/unload/reload response at multiple stretch rates and shows a less accurate prediction of the response for multi-step relaxation. This can be attributed to the highly non-linear relaxation behavior absent during cyclic loading. While we acknowledge this shortcoming, we save it for a future work.

Rate-independent		Rate-dependent	
Parameter	Value	Parameter	Value
G_0^{TI}(kPa)	199.26	$G_0^{\mathrm{TD}(1)}$(kPa)	4.99
$K(=10^3 G_0^{\mathrm{TI}})$(MPa)	199.26	$\tau^{(1)}$(s)	6.22
λ_L	2.04	$G_0^{\mathrm{TD}(2)}$(kPa)	0.58
A	0.45	$\tau^{(2)}$(s)	837.53
ν_{s0}	0.60	B	14.50
ν_{ss}	0.99	D	2.10
$R_0(s^{-1})$	N/A	n	1
		p	4.17
		a	0.02941
		$\dot{\Lambda}_0(s^{-1})$	10^{-4}

Table 1: DC745U calibrated material parameters.

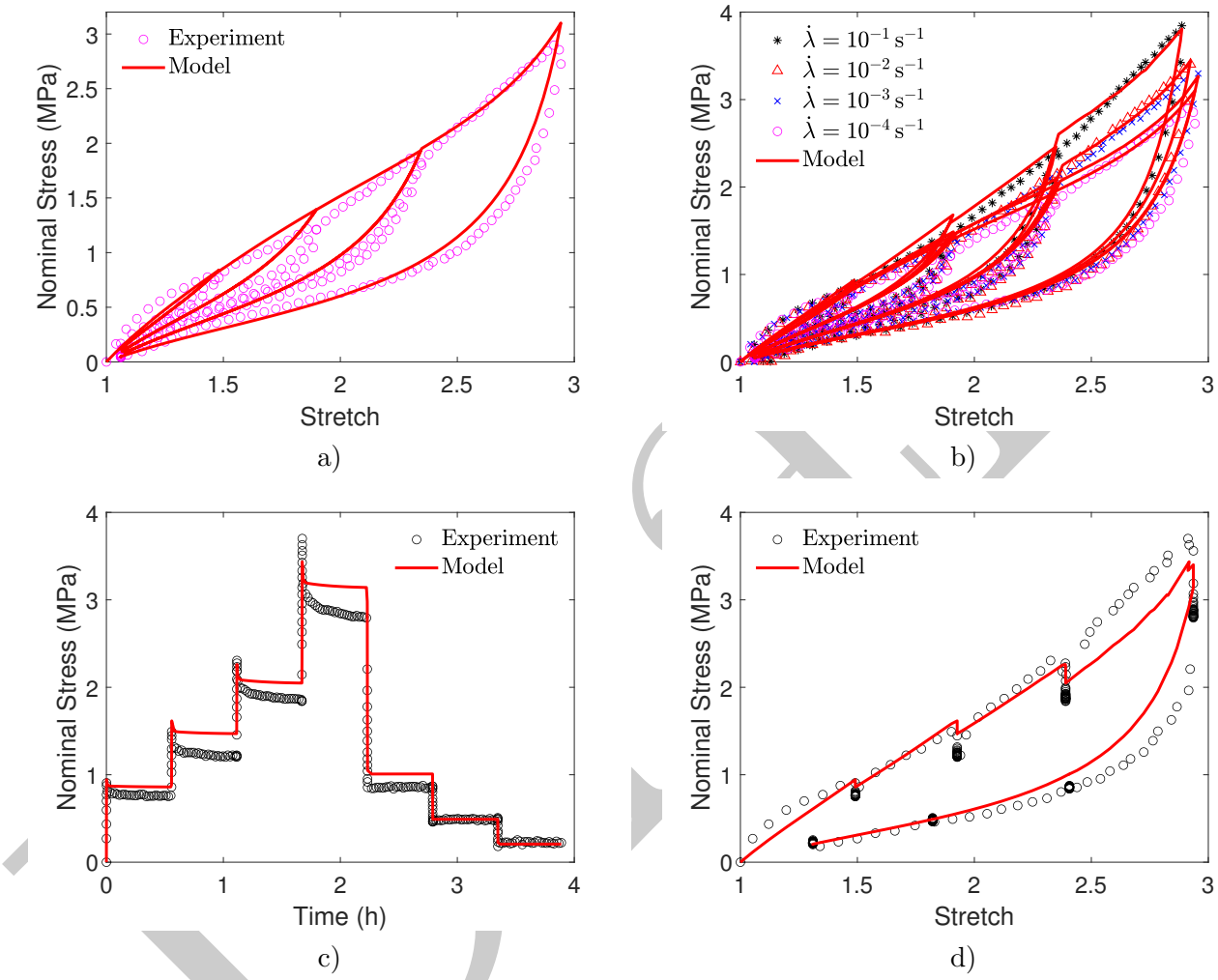

Figure 13: DC745U model calibration using virgin specimens, experiments are shown as open circles and the calibrated model as red solid lines. a) Quasi-static load/unload/reload, b) load/unload/reload at multiple stretch rates, and multi-step relaxation c) stress - time, and d) stress - stretch.

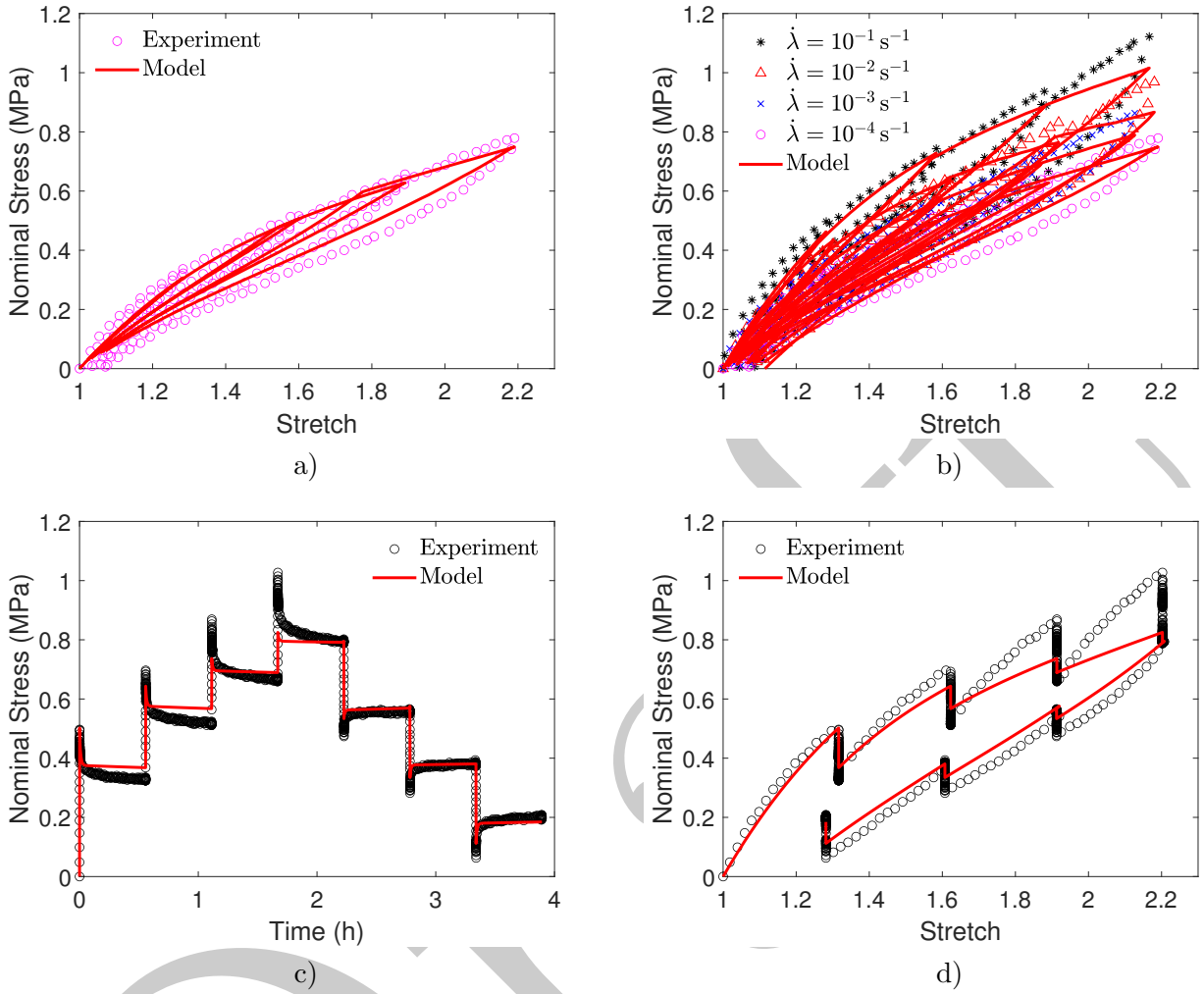

Figure 14: Buna 50A model calibration using virgin specimens, experiments are shown as open circles and the calibrated model as red solid lines. a) Quasi-static load/unload/reload, b) load/unload/reload at multiple stretch rates, and multi-step relaxation c) stress - time, and d) stress - stretch.

Rate-independent		Rate-dependent	
Parameter	Value	Parameter	Value
G_0^{TI}(kPa)	109.39	$G_0^{\mathrm{TD}(1)}$(kPa)	333.88
$K(=10^3 G_0^{\mathrm{TI}})$(MPa)	109.39	$\tau^{(1)}$(s)	24.06
λ_L	3	$G_0^{\mathrm{TD}(2)}$(kPa)	103.85
A	1.83	$\tau^{(2)}$(s)	8492.60
ν_{s0}	0.40	B	0.10
ν_{ss}	0.84	D	10.98
$R_0(s^{-1})$	-5.72×10^{-6}	n	1
		p	15.10
		a	7.26×10^{-7}
		$\dot{\Lambda}_0(s^{-1})$	10^{-4}

Table 2: Buna 50A calibrated material parameters.

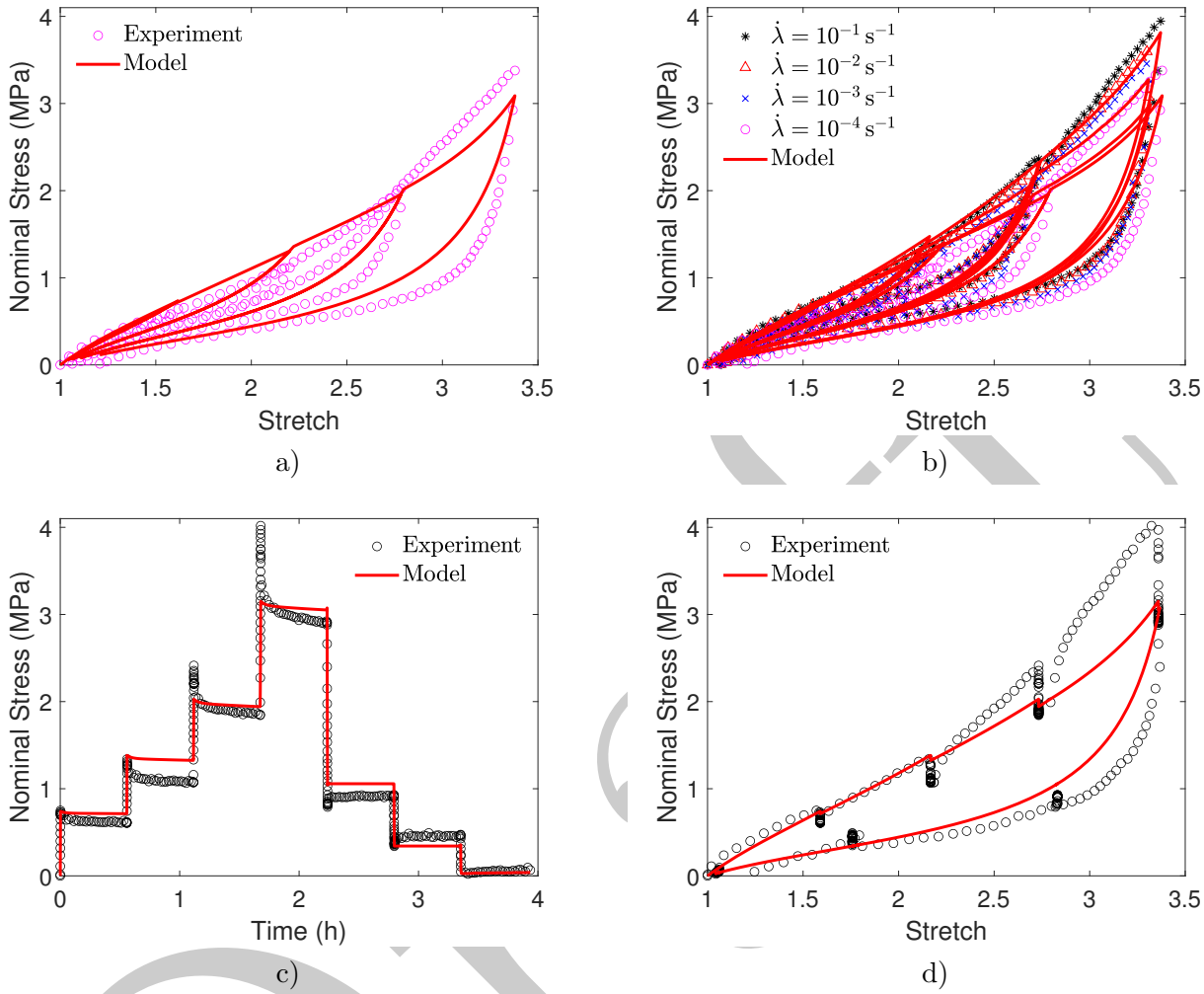

Figure 15: Neoprene 50A model calibration using virgin specimens, experiments are shown as open circles and the calibrated model as red solid lines. a) Quasi-static load/unload/reload, b) load/unload/reload at multiple stretch rates, and multi-step relaxation c) stress - time, and d) stress - stretch.

Rate-independent		Rate-dependent	
Parameter	Value	Parameter	Value
G_0^{TI}(kPa)	165.66	$G_0^{\mathrm{TD}(1)}$(kPa)	3.28
$K(=10^3 G_0^{\mathrm{TI}})$(MPa)	165.66	$\tau^{(1)}$(s)	93.29
λ_L	2.32	$G_0^{\mathrm{TD}(2)}$(kPa)	1.81
A	0.37	$\tau^{(2)}$(s)	3093.76
ν_{s0}	0.65	B	11.92
ν_{ss}	0.99	D	2.40
$R_0(s^{-1})$	N/A	n	1
		p	3.62
		a	5.5360×10^{-4}
		$\dot{\Lambda}_0(s^{-1})$	10^{-4}

Table 3: Neoprene 50A calibrated material parameters.

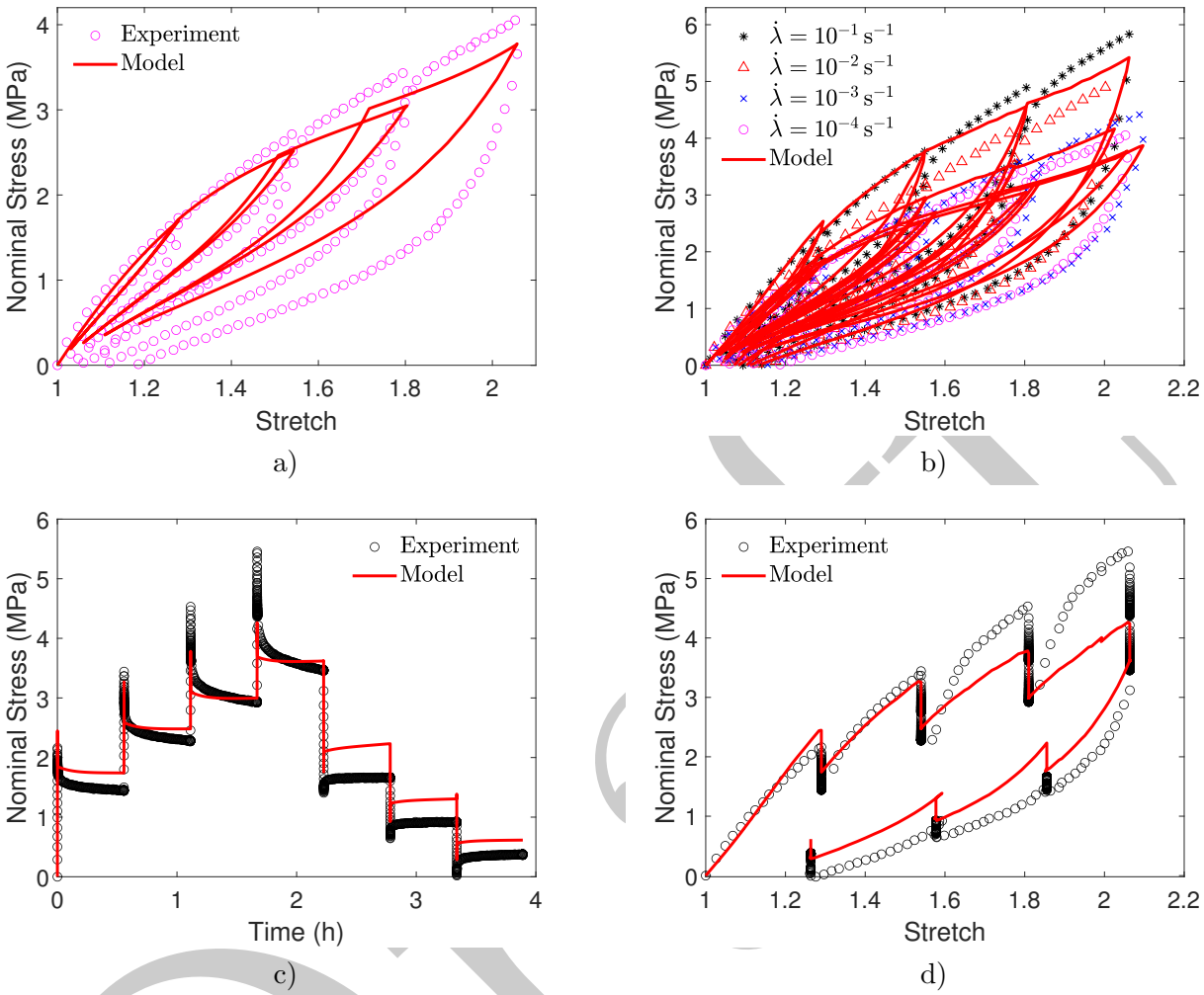

Figure 16: Neoprene 70A model calibration using virgin specimens, experiments are shown as open circles and the calibrated model as red solid lines. a) Quasi-static load/unload/reload, b) load/unload/reload at multiple stretch rates, and multi-step relaxation c) stress - time, and d) stress - stretch.

Rate-independent		Rate-dependent	
Parameter	Value	Parameter	Value
G_0^{TI}(kPa)	500	$G_0^{\mathrm{TD}(1)}$(kPa)	123.26
$K(=10^3 G_0^{\mathrm{TI}})$(MPa)	500	$\tau^{(1)}$(s)	2.06
λ_L	1.61	$G_0^{\mathrm{TD}(2)}$(kPa)	10.38
A	1.12	$\tau^{(2)}$(s)	372.87
ν_{s0}	0.48	B	5.00
ν_{ss}	0.99	D	1.60
$R_0(s^{-1})$	-4.01×10^{-6}	n	1
		p	3.77
		a	7.26×10^{-9}
		$\dot{\Lambda}_0(s^{-1})$	10^{-4}

Table 4: Neoprene 70A calibrated material parameters.

7 Validation

In order to validate our constitutive model, we perform inhomogeneous tension experiments at room temperature (24°C), and we compare the reaction force and strain fields between experimental and simulation results.

The specimen used for validation is prepared by extracting a dog bone sample using an ASTM D638-I cutting die from the provided material sheets. Then, three circular holes were punched out from the gauge section to create an inhomogeneous geometry, with a typical sample as shown in Figure 17a, with the exact drawings for each sample provided in Appendix A. Additionally, we spray paint the sample with a random speckle prior to the experiment, so that the full strain field can be measured using DIC. Once more, we perform tension test using the same uniaxial testing machine, and we measure the strain field using the DIC, and the force using the 500 N load cell.

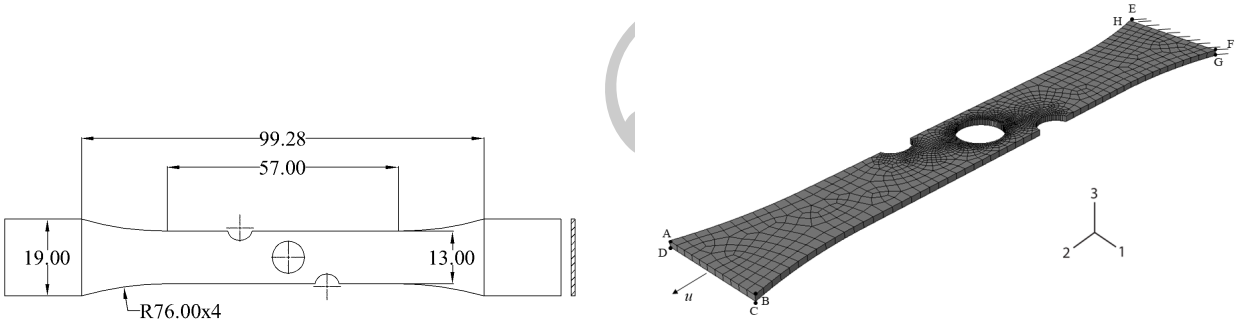

a) b)

Figure 17: a) Typical modified ASTM D638-I specimen used for the validation experiment with dimensions in mm, and b) corresponding undeformed initial finite element mesh with boundary conditions.

As for the simulations, we implemented the constitutive model in Abaqus/Standard (2023) by writing a user material subroutine UMAT. A typical mesh of the geometry shown in Figure 17b, however, the exact geometry and corresponding mesh was different for each material and was discretesized with:

- 1279 C3D8 elements, with a single element through the thickness for DC745U.
- 2570 C3D8 elements, with a two elements through the thickness for Buna 50A.
- 1408 C3D8 elements, with a single element through the thickness for Neoprene 50A.

- 2708 C3D8 elements, with two elements through the thickness for Neoprene 70A.

Also, the boundary conditions can be observed from Figure 17b; face EFGH is pinned ($\mathbf{u}_1 = \mathbf{u}_2 = \mathbf{u}_3 = 0$) and the displacement u measured from the experiment is prescribed on face ABCD in the 2 direction and constrained in the other directions. The force is obtained by summing up the reaction force from each node in the 2 direction on face EFGH. All remaining faces are considered traction free.

The results of the validation are shown in Figures 18, 19, 20, and 21. The experimentally prescribed displacement as a function of time is shown in Figures 18a, 19a, 20a, 21a, and is used as an input for the prescribed displacement in the simulation. A comparison of both force-displacement and force-time curves is shown in Figures 18b, 19b, 20b, 21b, and 18c, 19c, 20c, 21c, respectively. From these results, one may clearly observe a good quantitative agreement between the experiment and the simulation.

Furthermore, Figures 22, 23, 24, and 25 also show a good quantitative agreement between the experimental measured and simulated Hencky strain field component E_{22}, where the Hencky strain is given by $\mathbf{E} = \ln \mathbf{U}$ at various times.

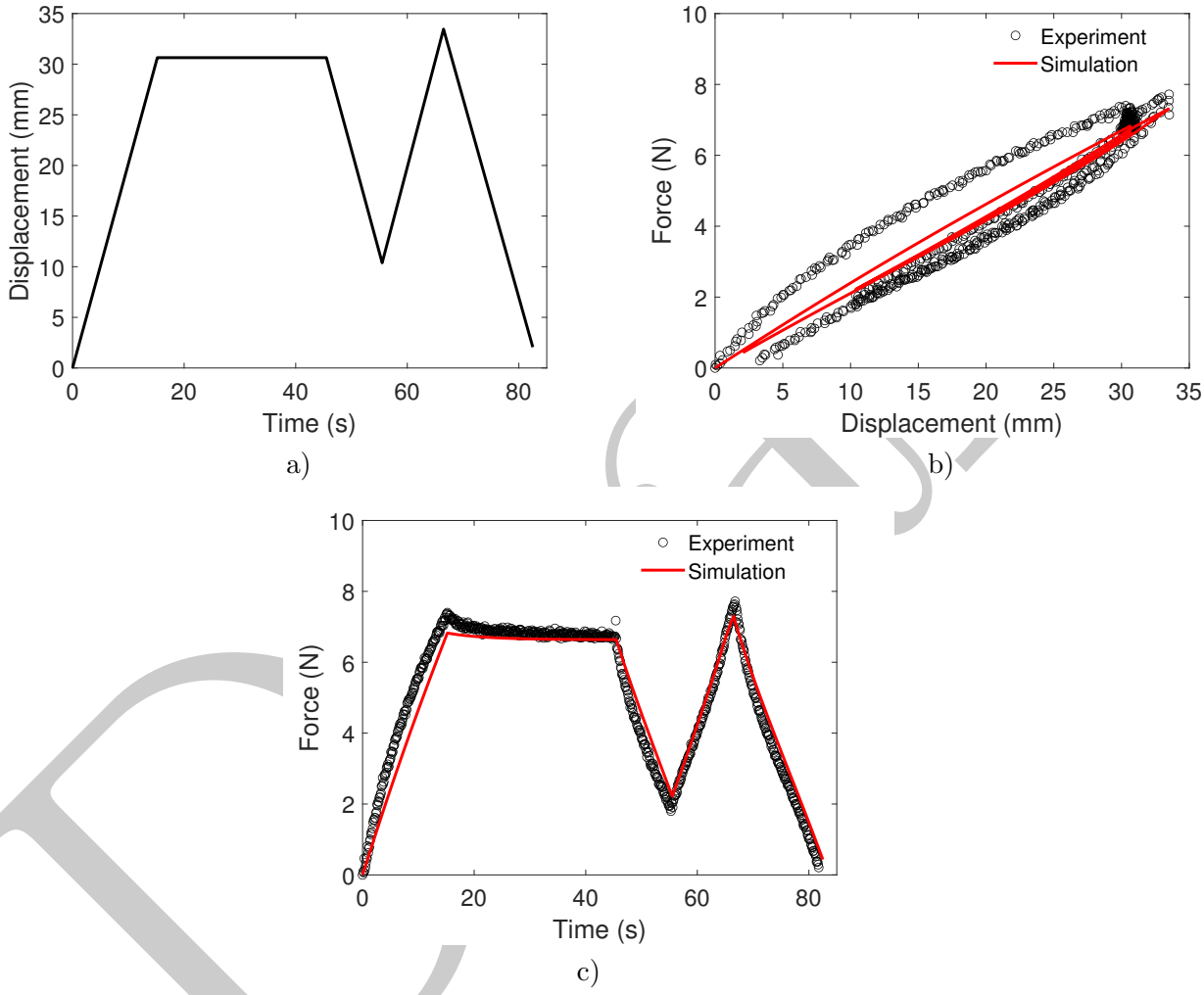

Figure 18: DC745U uniaxial model validation (Experiment and simulation comparison). a) Prescribed displacement profile. b) Force-displacement curve. c) Force-time curve.

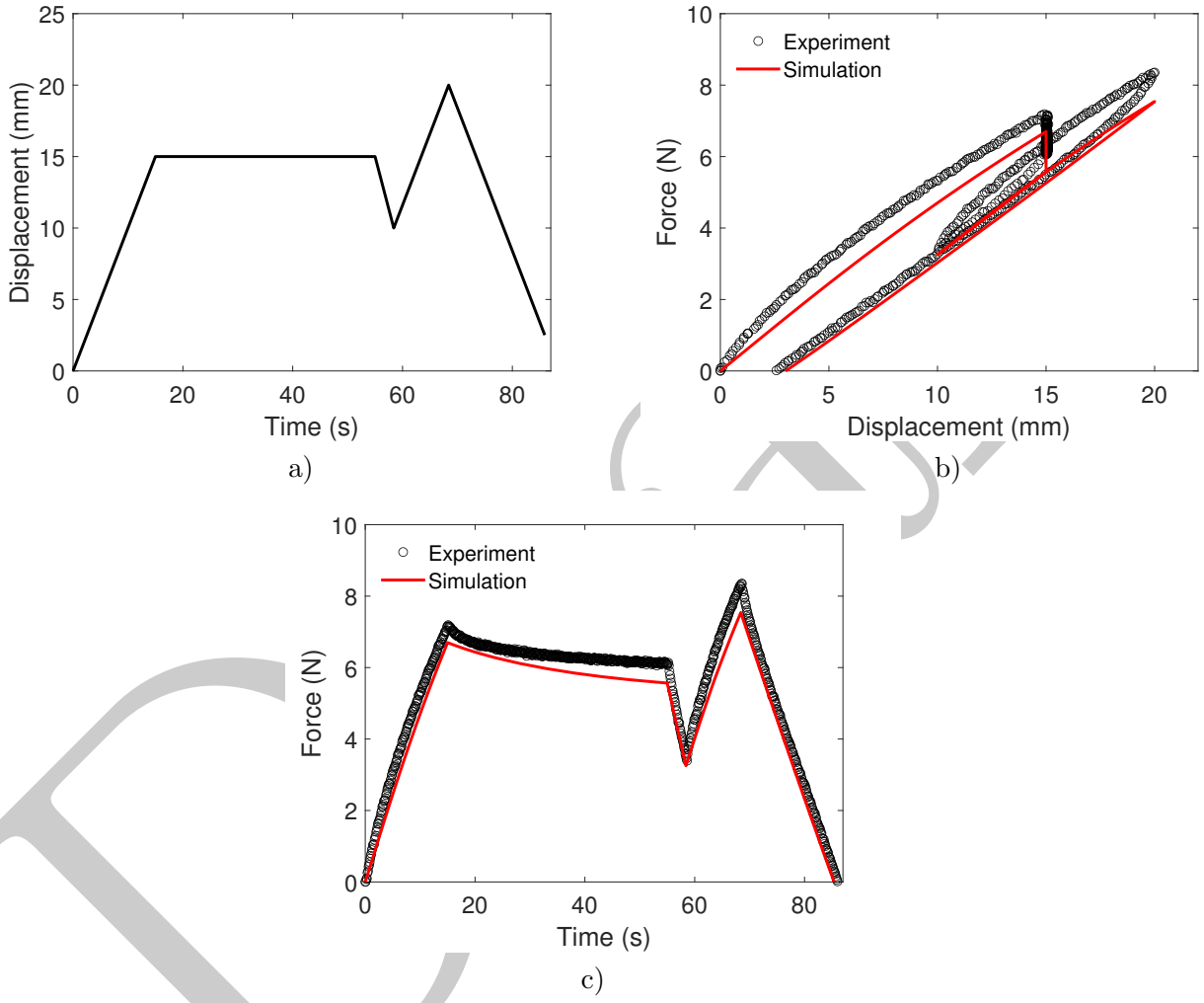

Figure 19: Buna 50A uniaxial model validation (Experiment and simulation comparison). a) Prescribed displacement profile. b) Force-displacement curve. c) Force-time curve.

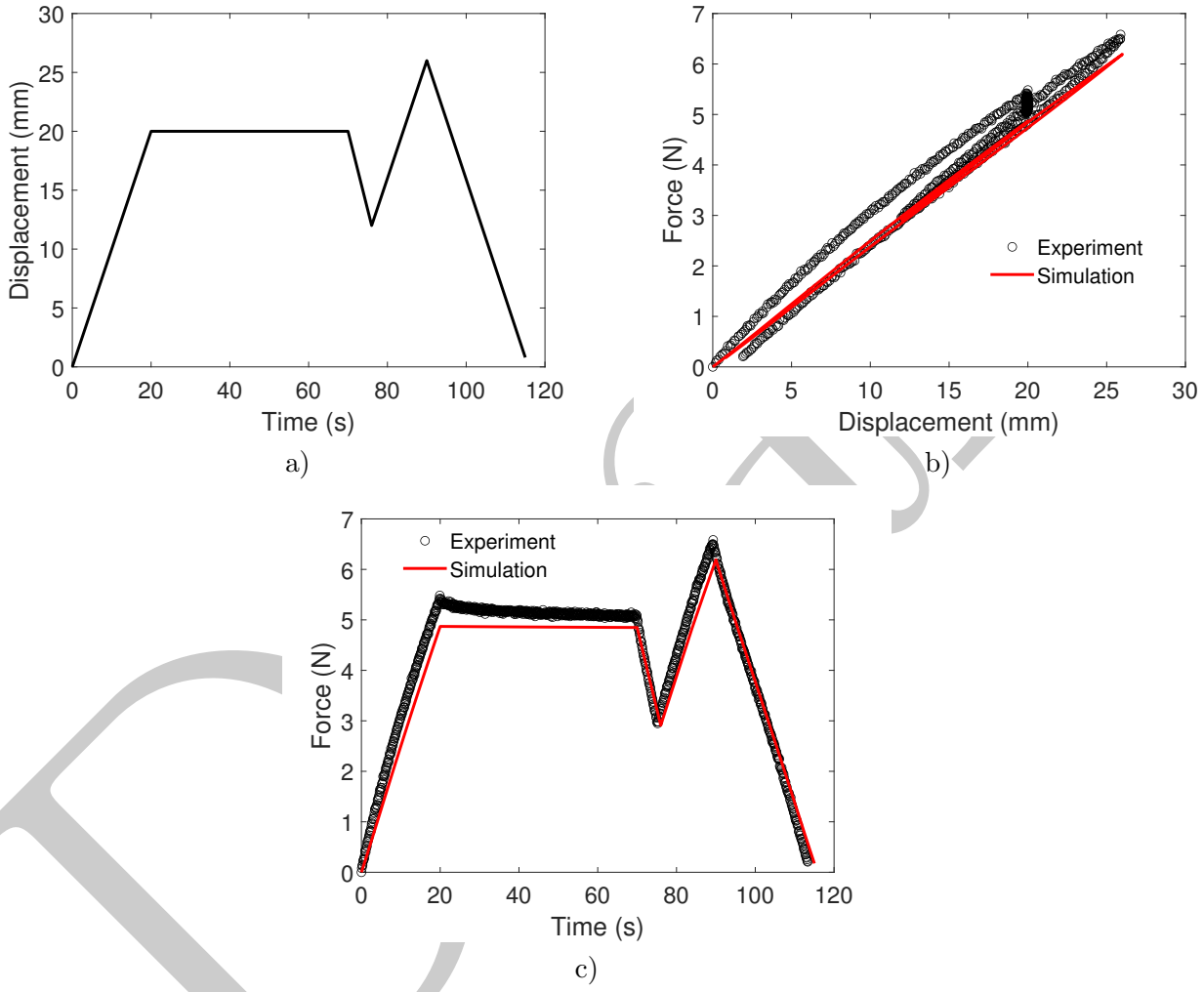

Figure 20: Neoprene 50A uniaxial model validation (Experiment and simulation comparison). a) Prescribed displacement profile. b) Force-displacement curve. c) Force-time curve.

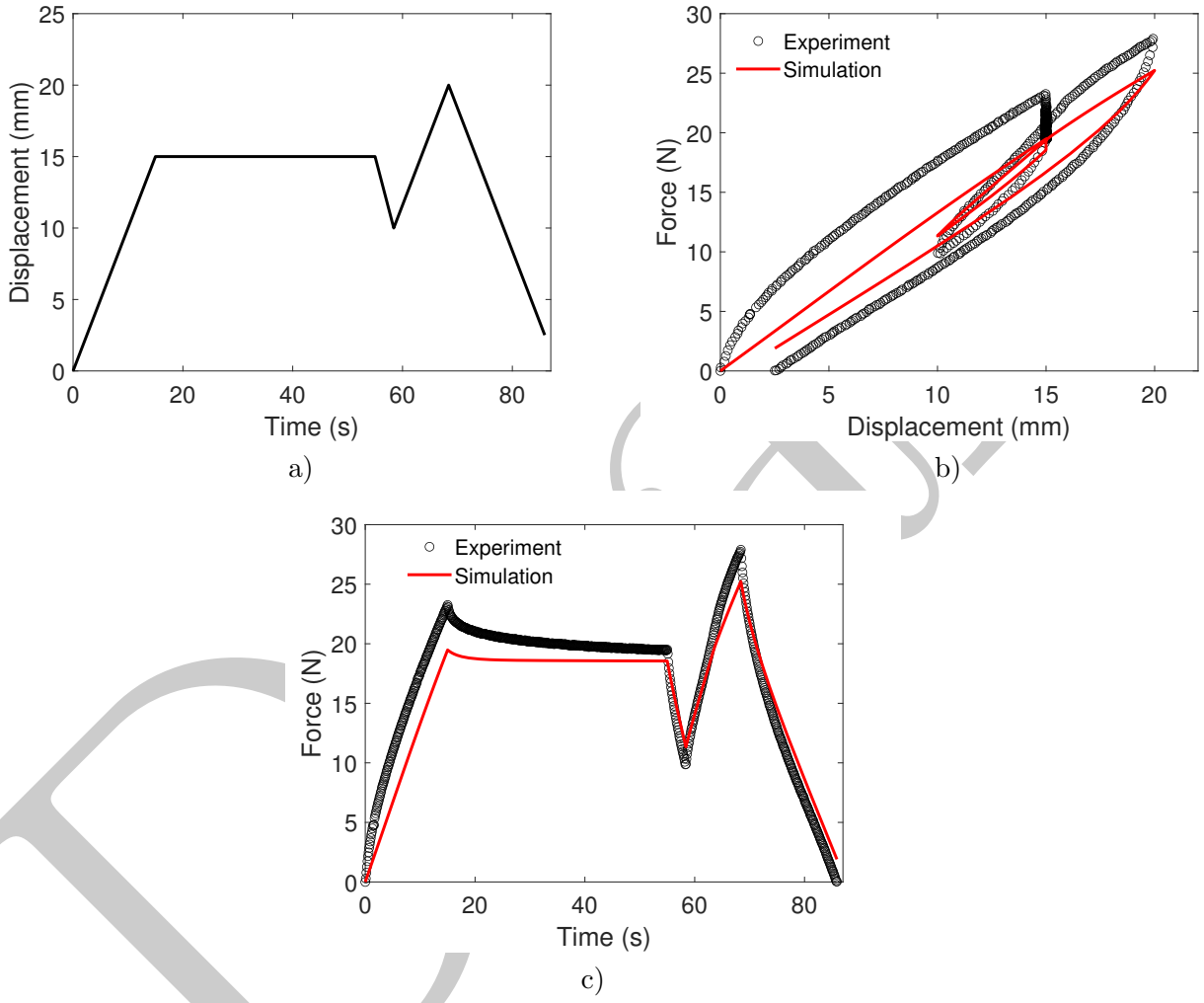

Figure 21: Neoprene 70A uniaxial model validation (Experiment and simulation comparison). a) Prescribed displacement profile. b) Force-displacement curve. c) Force-time curve.

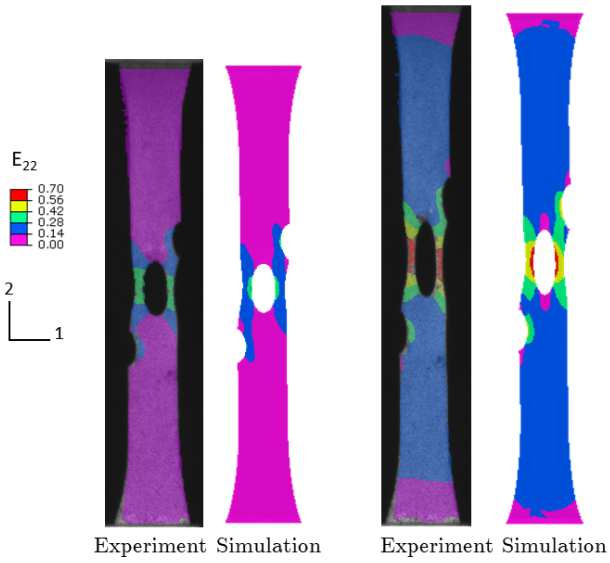

Figure 22: DC745U comparison of E_{22} for the inhomogeneous uniaxial deformation between the experimentally measured and simulated validation at a displacement of a) 13 mm, and b) 27 mm.

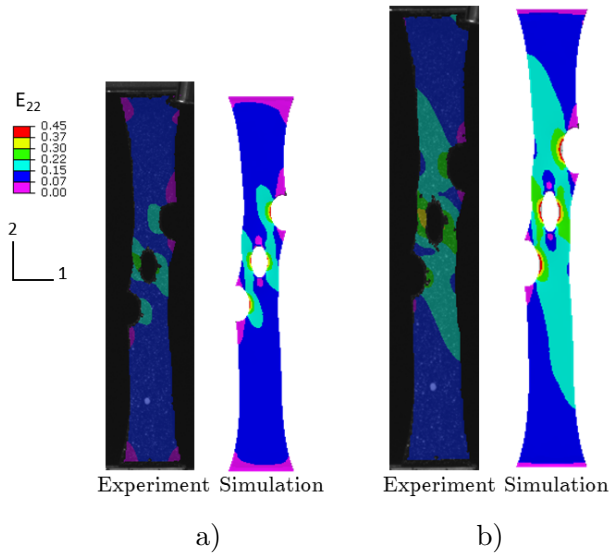

Figure 23: Buna 50A comparison of E_{22} for the inhomogeneous uniaxial deformation between the experimentally measured and simulated validation at a displacement of a) 15 mm, and b) 19.8 mm.

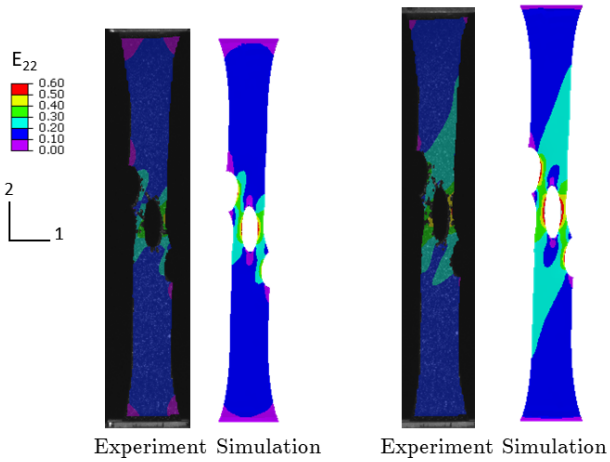

Figure 24: Neoprene 50A comparison of E_{22} for the inhomogeneous uniaxial deformation between the experimentally measured and simulated validation at a displacement of a) 20 mm, and b) 25.74 mm.

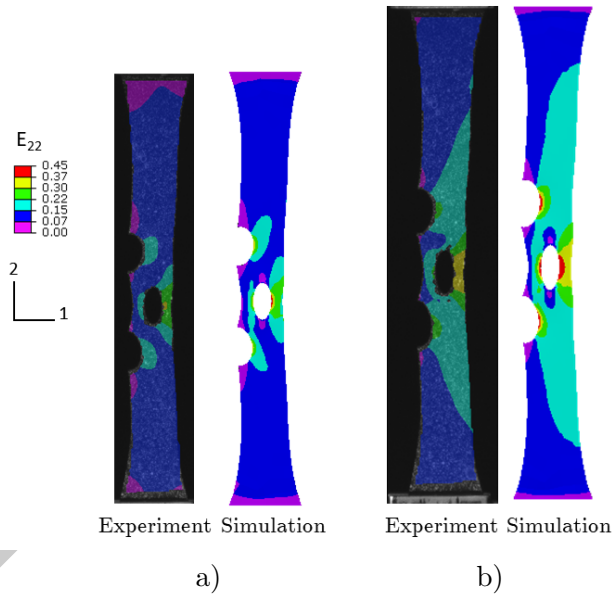

Figure 25: Neoprene 70A comparison of E_{22} for the inhomogeneous uniaxial deformation between the experimentally measured and simulated validation at a displacement of a) 15 mm, and b) 19.87 mm.

8 Conclusion

In this work we experimentally measured and numerically modeled the low to moderate constitutive behavior of filled viscoelastomers, specifically, DC745U, Buna 50A, Neoprene 50A, and Neoprene 70A with an emphasis on the concurrent viscoelastic and stress softening behavior.

The rather complex behavior was experimentally investigated by conducting a suite of large deformation uniaxial tests, such as load/unload/reload at multiple stretch rates and multi-step relaxation tests. Those tests were performed on both virgin and preconditioned specimens. The novel experimental contribution is that we have observed circumstantial evidence that the mechanisms that cause the Mullins effect appear to be the main drivers of viscoelasticity. We also observed that the inelastic mechanisms are more dominant during loading, and that all materials used in this work exhibit a stretch-stretch rate stiffening of the viscous response. There was also clear evidence that preconditioned samples exhibited recovery of the Mullins effect at room temperature, for some of the materials used.

For the constitutive model, we make use of the phenomenological approach that adapts the concept of phase change in a filled viscoelastomer for Mullins effect, coupled with a micro-mechanically motivated viscoelastic model. We specifically adopt an additive decomposition of the free energy to capture the combined stress-softening and stretch-stretch rate stiffening of the viscous response. The model was then calibrated against uniaxial tensile tests using non-linear least squares, and then implemented in the commercial finite element software Abaqus/Standard (2023) as a user material subroutine. Lastly, the model was validated reasonably, but not flawlessly, by performing inhomogeneous experiments and simulations, and comparing various quantities such as the reaction force to a prescribed displacement.

While much has been learned over the past decades, we believe there is further research to consider for this particular class of materials. Although the focus of this study is to investigate the mechanical behavior at room temperature, the literature indicates that temperature clearly has an affect on the mechanical behavior for this class of materials. Moreover, it is well known that Mullins effect may be recovered after prolonged times at elevated temperatures and other such conditions. For that reason, it remains an open question to understand the effect of temperature, on the coupling between the Mullins effect and viscoelasticity.

CRediT authorship contribution statement

Keven Alkhoury: Investigation, Writing - Original Draft. **Robert Ivko**: Investigation, Writing - Review & Editing. **Siva Nadimpalli**: Supervision, Writing - Review & Editing. **Mokarram Hossain**: Writing - Review & Editing. **Shawn A. Chester**: Supervision, Writing - Review & Editing.

Acknowledgements

SAC acknowledges partial support from the National Science Foundation under grant number (CMMI-1751520), and that this work was performed in part at NJIT under Subcontract No. B644387 under the auspices of the U.S. Department of Energy in collaboration with Lawrence Livermore National Laboratory under Contract DE-AC52-07NA27344 (LLNL-JRNL-858499-DRAFT). SN acknowledges partial support from the National Science Foundation under grant numbers (CMMI-1652409) and (CMMI-2026717). The opinions, findings, and conclusions, or recommendations expressed are those of the author(s) and do not necessarily reflect the views of the National Science Foundation. MH acknowledges the support of the Royal Society (UK) through the International Exchange Grant (IEC/NSFC/211316).

A Appendix: Detailed geometry of validation samples

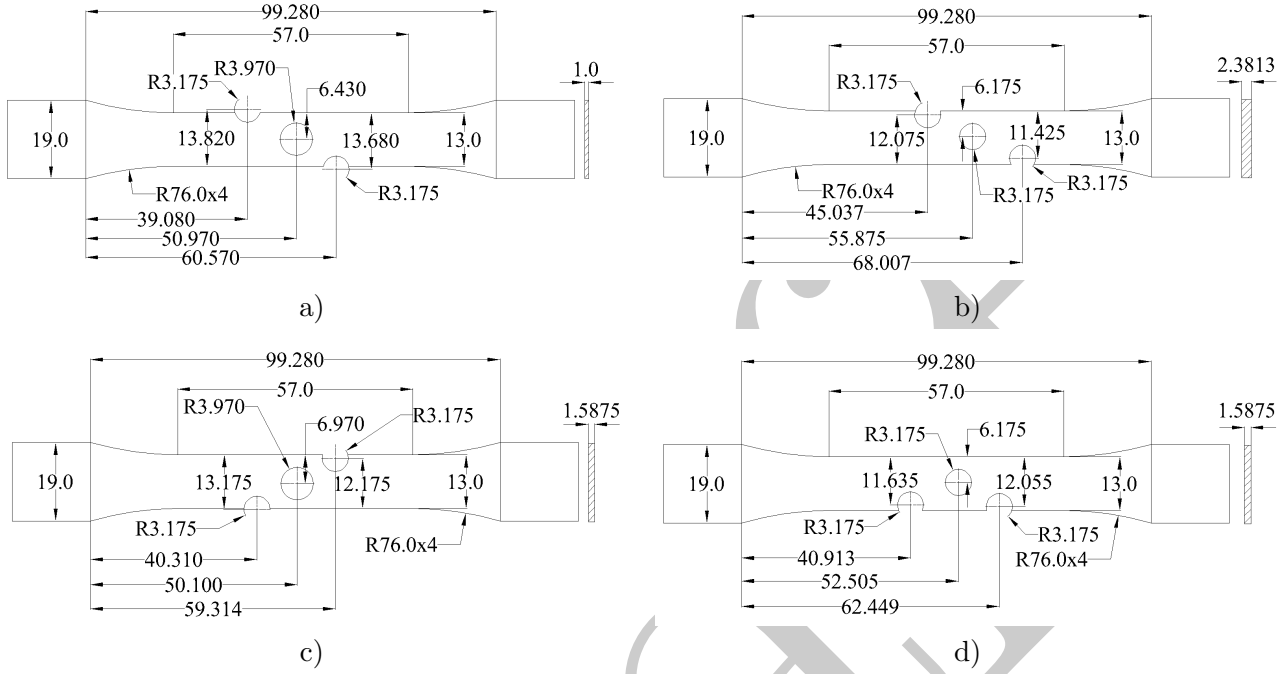

Figure 26: Detailed geometry of the samples used for the validation experiments. a) DC745U, b) Buna 50A, c) Neoprene 50A, and d) Neoprene 70A. All dimensions are in mm.

References

Abaqus/Standard. *Abaqus Reference Manuals*. Dassaults Systemes Simulia, Providence, RI, 2023.

A. Amin, A. Lion, S. Sekita, and Y. Okui. Nonlinear dependence of viscosity in modeling the rate-dependent response of natural and high damping rubbers in compression and shear: Experimental identification and numerical verification. *International Journal of Plasticity*, 22(9):1610–1657, 2006.

A. Amin, A. Bhuiyan, T. Hossain, and Y. Okui. Nonlinear viscosity law in finite-element analysis of high damping rubber bearings and expansion joints. *Journal of Engineering Mechanics*, 141 (6):04014169, 2015.

A. Anssari-Benam, R. Akbari, and R. Dargazany. Extending the theory of pseudo-elasticity to capture the permanent set and the induced anisotropy in the mullins effect. *International Journal of Non-Linear Mechanics*, 156:104500, 2023.

J. S. Bergström and M. C. Boyce. Constitutive modeling of the large strain time-dependent behavior of elastomers. *J. Mech. Phys. Solids*, 46(5):931–954, 1998. ISSN 0022-5096. doi: https://doi.org/10.1016/S0022-5096(97)00075-6. URL `https://www.sciencedirect.com/science/article/pii/S0022509697000756`.

J. S. Bergstrom and M. C. Boyce. Mechanical behavior of particle filled elastomers. *Rubber Chem. Technol.*, 72(4):633–656, 1999.

J. Bergström and M. Boyce. Large strain time-dependent behavior of filled elastomers. *Mechanics of Materials*, 32(11):627–644, 2000. ISSN 0167-6636. doi: https://doi.org/10.1016/S0167-6636(00)00028-4. URL `https://www.sciencedirect.com/science/article/pii/S0167663600000284`.

T. B. Birmingham, J. F. Kramer, J. T. Inglis, C. A. Mooney, L. J. Murray, P. J. Fowler, and S. Kirkley. Effect of a neoprene sleeve on knee joint position sense during sitting open kinetic chain and supine closed kinetic chain tests. *The American journal of sports medicine*, 26(4): 562–566, 1998.

A. F. Blanchard and D. Parkinson. Breakage of carbon-rubber networks by applied stress. *Rubber Chem. Technol.*, 25(4):808–842, 1952.

H. Bouasse and Z. Carrière. Sur les courbes de traction du caoutchouc vulcanisé. In *Annales de la Faculté des sciences de Toulouse: Mathématiques*, volume 5, pages 257–283, 1903.

F. Bueche. Molecular basis for the Mullins effect. *J. Appl. Polym. Sci.*, 4(10):107–114, 1960.

L. Chen, L. Wu, L. Song, Z. Xia, Y. Lin, W. Chen, and L. Li. The recovery of nano-sized carbon black filler structure and its contribution to stress recovery in rubber nanocomposites. *Nanoscale*, 12(48):24527–24542, 2020.

S. K. Clark. *Mechanics of pneumatic tires*. US Government Printing Office, 1981.

J. Diani, B. Fayolle, and P. Gilormini. A review on the Mullins effect. *Eur. Polym. J.*, 45(3): 601–612, mar 2009. ISSN 0014-3057. doi: 10.1016/J.EURPOLYMJ.2008.11.017.

A. Dorfmann and R. W. Ogden. A pseudo-elastic model for loading, partial unloading and reloading of particle-reinforced rubber. *Int. J. Solids Struct.*, 40(11):2699–2714, 2003.

A. Dorfmann and R. W. Ogden. A constitutive model for the Mullins effect with permanent set in particle-reinforced rubber. *Int. J. Solids Struct.*, 41(7):1855–1878, 2004.

S. Govindjee and J. Simo. A micro-mechanically based continuum damage model for carbon black-filled rubbers incorporating Mullins' effect. *J. Mech. Phys. Solids*, 39(1):87–112, 1991.

M. S. Green and A. V. Tobolsky. A new approach to the theory of relaxing polymeric media. *J. Chem. Phys.*, 14(2):80–92, 1946.

E. Guth. Theory of filler reinforcement. *Rubber Chem. Technol.*, 18(3):596–604, 1945.

J. A. C. Harwood and A. R. Payne. Stress softening in natural rubber vulcanizates. Part III. Carbon black-filled vulcanizates. *J. Appl. Polym. Sci.*, 10(2):315–324, 1966.

J. A. C. Harwood, L. Mullins, and A. R. Payne. Stress softening in natural rubber vulcanizates. Part II. Stress softening effects in pure gum and filler loaded rubbers. *J. Appl. Polym. Sci.*, 9 (9):3011–3021, 1965.

K. Hashimoto, A. Maeda, K. Hosoya, and Y. Todani. Specialty elastomers for automotive applications. *Rubber chemistry and technology*, 71(3):449–519, 1998.

L. Herrington, C. Simmonds, and J. Hatcher. The effect of a neoprene sleeve on knee joint position sense. *Research in Sports Medicine*, 13(1):37–46, 2005.

G. A. Holzapfel and J. C. Simo. A new viscoelastic constitutive model for continuous media at finite thermomechanical changes. *Int. J. Solids Struct.*, 33(20):3019–3034, 1996. ISSN 0020-7683. doi: https://doi.org/10.1016/0020-7683(95)00263-4. URL `https://www.sciencedirect.com/science/article/pii/0020768395002634`.

M. Hossain and Z. Liao. An additively manufactured silicone polymer: Thermo-viscoelastic experimental study and computational modelling. *Additive Manufacturing*, 35:101395, 2020. ISSN 2214-8604. doi: https://doi.org/10.1016/j.addma.2020.101395. URL `https://www.sciencedirect.com/science/article/pii/S2214860420307673`.

M. Hossain, R. Navaratne, and D. Perić. 3d printed elastomeric polyurethane: Viscoelastic experimental characterizations and constitutive modelling with nonlinear viscosity functions. *International Journal of Non-Linear Mechanics*, 126:103546, 2020. ISSN 0020-7462. doi: https://doi.org/10.1016/j.ijnonlinmec.2020.103546. URL `https://www.sciencedirect.com/science/article/pii/S0020746220302080`.

R. Houwink. Slipping of molecules during the deformation of reinforced rubber. *Rubber Chem. Technol.*, 29(3):888–893, 1956.

M. Klüppel and J. Schramm. A generalized tube model of rubber elasticity and stress softening of filler reinforced elastomer systems. *Macromol. theory simulations*, 9(9):742–754, 2000.

J. L. Leblanc. Rubber–filler interactions and rheological properties in filled compounds. *Prog. Polym. Sci.*, 27(4):627–687, may 2002. ISSN 0079-6700. doi: 10.1016/S0079-6700(01)00040-5.

M. Lerman. Orthopedic supports and material for making same, May 23 1989. US Patent 4,832,010.

Y. Li, B. Wang, and X. Gong. Modelling the mullins effect and the magnetic-dependent nonlinear viscoelasticity of isotropic soft magnetorheological elastomers. *International Journal of Solids and Structures*, 283:112475, 2023.

Z. Liao, M. Hossain, and X. Yao. Ecoflex polymer of different shore hardnesses: Experimental investigations and constitutive modelling. *Mechanics of Materials*, 144:103366, 2020a. ISSN 0167-6636. doi: https://doi.org/10.1016/j.mechmat.2020.103366. URL https://www.sciencedirect.com/science/article/pii/S016766362030020X.

Z. Liao, M. Hossain, X. Yao, R. Navaratne, and G. Chagnon. A comprehensive thermo-viscoelastic experimental investigation of ecoflex polymer. *Polymer Testing*, 86:106478, 2020b. ISSN 0142-9418. doi: https://doi.org/10.1016/j.polymertesting.2020.106478. URL https://www.sciencedirect.com/science/article/pii/S0142941820301185.

Z. Liao, J. Yang, M. Hossain, G. Chagnon, L. Jing, and X. Yao. On the stress recovery behaviour of ecoflex silicone rubbers. *International Journal of Mechanical Sciences*, 206: 106624, 2021. ISSN 0020-7403. doi: https://doi.org/10.1016/j.ijmecsci.2021.106624. URL https://www.sciencedirect.com/science/article/pii/S0020740321003581.

C. Linder, M. Tkachuk, and C. Miehe. A micromechanically motivated diffusion-based transient network model and its incorporation into finite rubber viscoelasticity. *J. Mech. Phys. Solids*, 59 (10):2134–2156, 2011.

A. Lion. A constitutive model for carbon black filled rubber: experimental investigations and mathematical representation. *Contin. Mech. Thermodyn.*, 8(3):153–169, 1996.

A. Lion. A physically based method to represent the thermo-mechanical behaviour of elastomers. *Acta Mech.*, 123(1-4):1–25, 1997. doi: 10.1007/BF01178397.

T. Lu, J. Wang, R. Yang, and T. Wang. A constitutive model for soft materials incorporating viscoelasticity and mullins effect. *Journal of Applied Mechanics*, 84(2):021010, 2017.

J. Lubliner. A model of rubber viscoelasticity. *Mech. Res. Commun.*, 12(2):93–99, 1985. ISSN 0093-6413. doi: https://doi.org/10.1016/0093-6413(85)90075-8. URL https://www.sciencedirect.com/science/article/pii/0093641385900758.

Y. Mao, S. Lin, X. Zhao, and L. Anand. A large deformation viscoelastic model for double-network hydrogels. *J. Mech. Phys. Solids*, 100:103–130, mar 2017. ISSN 0022-5096. doi: 10.1016/J.JMPS.2016.12.011.

G. Marckmann, E. Verron, L. Gornet, G. Chagnon, P. Charrier, and P. Fort. A theory of network alteration for the Mullins effect. *J. Mech. Phys. Solids*, 50(9):2011–2028, 2002.

C. Miehe. Discontinuous and continuous damage evolution in Ogden-type large-strain elastic materials. *Eur. J. Mech. A. Solids*, 14(5):697–720, 1995.

C. Miehe and S. Göktepe. A micro–macro approach to rubber-like materials. Part II: The micro-sphere model of finite rubber viscoelasticity. *J. Mech. Phys. Solids*, 53(10): 2231–2258, 2005. ISSN 0022-5096. doi: https://doi.org/10.1016/j.jmps.2005.04.006. URL `https://www.sciencedirect.com/science/article/pii/S0022509605000918`.

L. Mullins. Effect of Stretching on the Properties of Rubber. *Rubber Chem. Technol.*, 21:281–300, 1948.

L. Mullins and N. R. Tobin. Theoretical model for the elastic behavior of filler-reinforced vulcanized rubbers. *Rubber Chem. Technol.*, 30(2):555–571, 1957.

L. Mullins and N. R. Tobin. Stress softening in rubber vulcanizates. Part I. Use of a strain amplification factor to describe the elastic behavior of filler-reinforced vulcanized rubber. *J. Appl. Polym. Sci.*, 9(9):2993–3009, 1965.

R. W. Ogden and D. G. Roxburgh. A pseudo–elastic model for the Mullins effect in filled rubber. *Proc. R. Soc. London. Ser. A Math. Phys. Eng. Sci.*, 455(1988):2861–2877, 1999.

A. R. Payne. The dynamic properties of carbon black loaded natural rubber vulcanizates. Part II. *J. Appl. Polym. Sci.*, 6(21):368–372, 1962. doi: https://doi.org/10.1002/app.1962.070062115. URL `https://onlinelibrary.wiley.com/doi/abs/10.1002/app.1962.070062115`.

J. Plagge and M. Klüppel. Mullins effect revisited: Relaxation, recovery and high-strain damage. *Materials Today Communications*, 20:100588, 2019. ISSN 2352-4928. doi: https://doi.org/10.1016/j.mtcomm.2019.100588. URL `https://www.sciencedirect.com/science/article/pii/S235249281930546X`.

H. J. Qi and M. C. Boyce. Constitutive model for stretch-induced softening of the stress–stretch behavior of elastomeric materials. *J. Mech. Phys. Solids*, 52(10):2187–2205, 2004.

S. Reese and S. Govindjee. A theory of finite viscoelasticity and numerical aspects. *Int. J. Solids Struct.*, 35(26):3455–3482, 1998. ISSN 0020-7683. doi: https://doi.org/10.1016/S0020-7683(97)00217-5. URL https://www.sciencedirect.com/science/article/pii/S0020768397002175.

B. P. Reis, L. M. Nogueira, D. A. Castello, and L. A. Borges. A visco-hyperelastic model with mullins effect for polyurethane elastomers combining a phenomenological approach with macromolecular information. *Mechanics of Materials*, 161:104023, 2021.

J. C. Simo. On a fully three-dimensional finite-strain viscoelastic damage model: formulation and computational aspects. *Comput. Methods Appl. Mech. Eng.*, 60(2):153–173, 1987.

H. So and U. D. Chen. A nonlinear mechanical model for solid-filled rubbers. *Polym. Eng. & Sci.*, 31(6):410–416, 1991. doi: https://doi.org/10.1002/pen.760310605. URL https://onlinelibrary.wiley.com/doi/abs/10.1002/pen.760310605.

H. Toopchi-Nezhad, M. J. Tait, and R. G. Drysdale. Lateral response evaluation of fiber-reinforced neoprene seismic isolators utilized in an unbonded application. *Journal of Structural Engineering*, 134(10):1627–1637, 2008.

T. R. Vijayaram. A technical review on rubber. *International Journal on Design and Manufacturing Technologies*, 3(1):25–37, 2009.

S. Wang and S. A. Chester. Modeling thermal recovery of the mullins effect. *Mechanics of Materials*, 126:88–98, 2018a. ISSN 0167-6636. doi: https://doi.org/10.1016/j.mechmat.2018.08.002. URL https://www.sciencedirect.com/science/article/pii/S0167663618301066.

S. Wang and S. A. Chester. Experimental characterization and continuum modeling of inelasticity in filled rubber-like materials. *Int. J. Solids Struct.*, 136-137:125–136, apr 2018b. ISSN 00207683. doi: 10.1016/j.ijsolstr.2017.12.010.

L. Yan, D. A. Dillard, R. L. West, L. D. Lower, and G. V. Gordon. Mullins effect recovery of a nanoparticle-filled polymer. *Journal of Polymer Science Part B: Polymer Physics*, 48(21): 2207–2214, 2010.